Nipah virus Bangladesh infection elicits organ-specific innate and inflammatory responses in the marmoset model

Christian S. Stevens[1], Jake Lowry[2], Terry Juelich[3], Colm Atkins[3,#], Kendra Johnson[4], Jennifer K Smith[3], Maryline Panis[1], Tetsuro Ikegami[3], Benjamin tenOever[1], Alexander N. Freiberg[3], Benhur Lee[1]

[1]Icahn School of Medicine at Mount Sinai, Department of Microbiology

[2]University of Texas Medical Branch, Animal Resource Center

[3]University of Texas Medical Branch, Department of Pathology

[4]University of Texas Medical Branch, Department of Microbiology and Immunology

[#]Present address: Rutgers University, Department of Cell Biology and Neuroscience

Abstract. The common marmoset (*Callithrix jacchus*) has, in recent years, received more recognition as an ideal non-human primate (NHP) model not only for studies related to neuroscience, but also at high-biocontainment due to its smaller size and relative ease of handling. Here, we evaluated the susceptibility and pathogenesis of Nipah virus Bangladesh strain (NiV_B) infection in marmosets at biosafety level 4. Four marmosets were infected via the intranasal and intratracheal route and monitored for disease development. We obtained histopathological data, quantified genome copies on >25 tissue-types, and performed RNA-seq on six different organs from all infected and control marmosets. All four subjects developed fatal disease between days 8 and 11 post infection, with three animals developing pulmonary edema and hemorrhage as well as multi-focal hemorrhagic lymphadenopathy. One subject recapitulated neurologic clinical symptoms and cardiomyopathy on gross pathology. In all animals, syncytia were evident in endothelial cells in pulmonary vessels, cells in alveolar septum, and in splenic follicles or red pulp. To define the organ-specific innate and inflammatory responses, we performed RNA-seq on six different organs from all infected and compared to naïve non-infected marmoset tissues. RNA-seq gave 17.4 million reads per sample on average, with the most highly infected tissue sample, the lung of one

marmoset, containing >180,000 virus-specific reads. NiV V and W transcripts comprised ~40% of all phosphoprotein-derived transcripts with V and W being very close to each other proportionally. Principal component analysis showed that in brain stem, the marmoset exhibiting neurological symptoms displayed a unique RNA transcriptome relative even to other infected marmosets. Upregulated genes in the various tissues belonged to distinct GO pathways. Additionally, one male and female animal had detectable viral reads in their ovaries (27,120) and testes (858). Our results provide a more comprehensive understanding of NiV pathogenesis in an accessible and novel NHP model, closely reflecting clinical disease as observed in NiV patients.

Key words. Nipah virus Bangladesh; primate; common marmoset; pathogenesis; respiratory disease; neurological disease; cardiomyopathy; RNA-seq; inflammatory response

Introduction

Nipah virus (NiV), a zoonotic, bat-borne negative-sense paramyxovirus of the genus *Henipavirus*, first emerged in Malaysian 1998/1999 during an outbreak in pigs [1]. Since then, outbreaks have occurred almost every year, resulting in over 600 cases of respiratory and/or neurological disease in patients, with 59% percent of which resulted in death [2]. Two major clades, NiV-Malaysia (NiV_M) and NiV-Bangladesh (NiV_B), have since emerged. All but two outbreaks have been NiV_B, which has had a higher case fatality rate (CFR) of 76% relative to NiV_M which has had a CFR of 39% [2]. In addition to a higher observed CFR, NiV_B also has a shorter average incubation period, a higher rate of respiratory symptoms, including patients developing an acute respiratory distress syndrome, and a smaller proportion of patients exhibiting segmental myoclonus relative to NiV_M [3–5]. Another important difference has been the extent of human-to-human transmission, common in NiV_B outbreaks but extremely rare in NiV_M outbreaks [6]. Given these significant differences, and that NiV_B has made up all but two outbreaks to date, animal models successfully recapitulating NiV_B pathology in humans are especially critical.

Many animal models have been used to investigate NiV pathogenesis and vaccine research including cats (*Felis catus*), ferrets (*Mustela putorius furo*), golden hamsters (*Mesocricetus auratus*), guinea pigs (*Cavia porcellus*), pigs (*Sus scrofa domesticus*), and mice (*Mus musculus*) [7–19]. Additionally, several non-human primate (NHP) models have been explored: African green monkeys (*Chlorocebus aethiops*; AGM), cynomolgus macaques (*Macaca fascicularis*), squirrel monkeys (*Saimiri sciureus*), and grivets (*Chlorocebus aethiops*) [20–34]. Among these, only AGMs have been able to faithfully recapitulate the high lethality of NiV_B exposure as well as most other clinical signs. However, overt clinical signs of neurological disease are seen very rarely in AGMs despite neurological disease being commonly seen via MRI and post-mortem histopathology. Additionally, myocarditis has been consistently reported among patients infected with NiV_B but to date there have been no reports of myocarditis in any animal models [35].

65

66 NiV infection in NHP models consistently replicate much of the hallmark clinical pathology and
67 histopathology of NiV infection. Systemic vasculitis, hypoalbuminemia, pneumonitis, coagulopathy, and
68 congestion in the liver and spleen are commonly seen in AGMs [21,22], although models such as the
69 cynomolgus macaque are unable to replicate many of these signs [25]. Transcriptional profiling in AGMs
70 has also shown significant upregulation in innate immune signaling genes (*MX2*, *OASL, OAS2*),
71 particularly among non-survivors of infection relative to survivors [25]. Others have shown that NHP
72 models show an especially robust expression of interferon stimulated genes in the lung, including *ISG15*
73 and *OAS1*, [36]. Additionally, the success of the AGM model of NiV infection has given insight into the
74 peripheral immune response to infection. For example, while CD8+ T cell activation and proliferation
75 markers are drastically increased during infection, increased natural killer cell response was correlated
76 with improved survival [30].

77

78 Although AGMs are the current standard NHP model of NiV infection, they suffer from a few
79 shortcomings. Thus far there are few reports of overt clinical signs of neurological disease and no reports
80 of myocarditis in NiV_B-infected AGMs. Additionally, given the biosafety level 4 (BSL4) requirements of
81 working with NiV, AGMs large size and associated costs are historically a significant barrier. In order to
82 diversify the preclinical testing portfolio of NHP models, we show here that NiV_B infection of the common
83 marmoset (*Callithrix jacchus*) can faithfully recapitulate pathology seen in humans. Marmosets were
84 chosen because they have several distinct advantages. First, they are an ideal NHP model for studying
85 high-biocontainment human respiratory pathogens because of their small size—approximately 20-30
86 centimeters in body length and 250-400 grams in body weight—and relative ease of handling. Second,
87 they are the first among New World monkeys to have their whole genome sequenced and assembled
88 allowing for techniques like RNA-sequencing (RNA-seq) to elucidate RNA expression changes in infected
89 and uninfected tissues [37]. Lastly, marmosets provide other logistical advantages such as the ability to
90 perform transmission experiments given that they can be co-housed and a high reproductive efficiency

91 with a short gestation period and delivery interval allows for easier development of transgenic animals
92 [38]. With these advantages in mind, results of this study identified marmosets as a highly susceptible
93 novel new-world NHP model of NiV_B infection and pathogenesis.

Material and Methods

Ethics statement. Experiments were approved by the Institutional Animal Care and Use Committee of the University of Texas Medical Branch (UTMB) and performed following the guidelines of the Association for Assessment and Accreditation of Laboratory Animal Care International (AAALAC) by certified staff in an AAALAC-approved facility. Animals were co-housed in primate cages allowing social interactions, under controlled conditions of humidity, temperature and light (12-hour light/12-hour dark cycles). Animals were monitored pre- and post-infection and fed commercial monkey chow, treats and fruit twice daily. Food and water were available ad libitum and environmental enrichment consisted of commercial toys. All procedures were conducted by BSL4-trained personnel under the oversight of an attending BSL4-trained veterinarian. All invasive procedures described here were performed on animals under isoflurane anesthesia. Animals that reached euthanasia criteria were euthanized using a pentobarbital-based euthanasia solution.

Virus and cells. Nipah virus (Bangladesh strain, NiV_B; 200401066 isolate) was kindly provided by Dr. Thomas Ksiazek (UTMB). The virus was propagated on Vero E6 cells (ATCC, CRL1586) in Dulbecco's minimal essential medium (DMEM) supplemented with 5% fetal bovine serum (HyClone, Logan, UT), penicillin, and streptomycin at 37°C in a humidified CO_2 incubator (5%). Virus titers were determined by plaque assay on Vero cells (ATCC, CCL-81) as previously described [39]. All work with infectious virus was performed at BSL4 biocontainment at the Galveston National Laboratory (GNL) at UTMB.

Animal studies. Four healthy marmosets (2 females, 2 males; 348 to 453 gram) were inoculated with 6.33×10^4 plaque forming units (PFU) of NiV_B with the dose being equally divided between the intranasal (IN) and intratracheal (IT) routes for each animal. After infection, animals were closely monitored for signs of clinical illness, changes in body temperature (BMDS transponders) and body weight. A scoring system was utilized monitoring respiratory, food intake, responsiveness, and neurological parameters to

120 determine study endpoint. In addition, changes in blood chemistry and hematology were monitored. On
121 days -7, 1, 3, 5, 7, and 10 days post infection, blood was collected via the femoral vein and swabs (oral,
122 nasal, rectal).
123
124 **Hematology and serum biochemistry.** Blood was collected in tubes containing EDTA and complete
125 blood counts (CBC) were evaluated with a VetScan HM5. (Abaxis, Union City, CA). Hematological
126 analysis included total white blood cell counts, white blood cell differentials, red blood cell counts, platelet
127 counts, hematocrit values, total hemoglobin concentrations, mean cell volumes, mean corpuscular
128 volumes and mean corpuscular hemoglobin concentrations. Clinical chemistry analysis was performed
129 using a VetScan2 Chemistry Analyzer (Abaxis, Union City, CA). Serum samples were tested for
130 concentrations of albumin (ALB), amylase (AMY), alanine aminotransferase (ALT), alkaline phosphatase
131 (ALP), glucose (GLU), total protein (TP), total bilirubin (TBIL), plasma electrolytes (calcium, phosphorus,
132 sodium, and potassium, blood urea nitrogen (BUN), creatinine (CRE) and globulin (GLOB)).
133
134 **X-ray images.** X-ray images were obtained using the MinXray model HF 100/30 portable x-ray unit
135 (Northbrook, IL) operated at 78 kVp 12 3.20 mAs at a distance of 40 inches from the subject. A Fuji DR
136 14x17 inch panel served as the exposure plate and the images were processed in the SoundVet
137 application (Carlsbad, CA).
138
139 **Sample collection and RNA isolation.** Nasal, oral, and rectal swabs were collected in 1 ml of Dulbecco's
140 minimal essential medium (DMEM) (Sigma-Aldrich, St. Louis, MO) and vortexed for 30 s. Whole blood
141 was collected in EDTA Vacutainers (Beckman Dickinson, Franklin Lakes, NJ) for hematology and serum
142 biochemistry, while another part was mixed with TRIzol LS for RNA extraction. At time of euthanasia, full
143 necropsies were performed, and tissues were homogenized in TRIzol reagent (Qiagen, Inc.) using
144 Qiagen TissueLyser and stainless-steel beads. The liquid phase was transferred into a new cryovial and
145 stored at -80°C. The tissues sampled include bronchial lymph node, mandibular lymph node, mediastinal

146 lymph node, inguinal lymph node, salivary gland lymph node, axillary lymph node, mesenteric lymph
147 node, femoral bone marrow, tonsil, oro/nasopharynx, nasal mucosa, trachea, lung (left upper lobe, left
148 lower lobe, right upper lobe, right lower lobe), right bronchos, left bronchos, heart, liver, spleen, kidney,
149 adrenal gland, pancreas, jejunum, colon transversum, brachial plexus, brain (frontal, cerebellum, stem),
150 cervical spinal cord, pituitary gland, urinary bladder, and testes/ovaries. All blood samples and swabs
151 were inactivated in TRIzol LS and TRIzol reagent, respectively, prior to removal from the BSL4 laboratory.
152 Subsequently, RNA was isolated from blood and swabs using the QIAamp viral RNA kit (Qiagen, Inc.)
153 and from tissues using the RNeasy minikit (Qiagen, Inc.) according to the manufacturer's instructions
154 supplied with each kit.
155
156 **RT-qPCR.** RT-qPCR was used to quantitate viral loads in tissues, swabs and blood. RNA was extracted
157 from tissues homogenized in TRIzol reagent or from blood and swabs mixed with TRIzol LS reagent
158 using Direct-zol RNA Miniprep kits (Zymo Research, Irvine, CA). RT-qPCR assays were then run using
159 QuantiFast RT-PCR mix (Qiagen, Hilden, Germany), probes targeting NiV_M P gene (5′-
160 ACATACAACTGGACCCARTGGTT-3′ and 5′-CACCCTCTCTCAGGGCTTGA-3′) (IDT, Coralville, IA),
161 and fluorescent probe (5′-6FAM-ACAGACGTTGTATA + C + CAT + G-TMR) (TIB MOLBIOL, Adelphia,
162 NJ). RT-qPCR was performed using the following cycle: 10 minutes at 50 °C, 5 minutes at 95 °C, and 40
163 cycles of 10 seconds at 95 °C and 30 seconds at 60 °C using a BioRad CFX96 real time system. Assays
164 were run in parallel with uninfected hamster tissues and a NiV_M stock standard curve.
165
166 **Virus titration.** Virus titration was performed by plaque assay on Vero cells as previously described [39].
167
168 **Histopathology and immunohistochemistry.** Necropsies were performed on euthanized animals, and
169 tissues collected for histopathology and immunohistochemistry. Tissues were immersion-fixed in 10%
170 neutral buffered formalin for at least 21 days under BSL-4 conditions with regular formalin changes.
171 Specimens were then processed under BSL-2 conditions. Briefly, tissues were dehydrated through a

172 series of graded ethanol baths, infiltrated by and embedded with paraffin wax, sectioned at 5 μm
173 thickness, and stained with hematoxylin and eosin. Immunohistochemistry for NiV nucleoprotein
174 detection was performed using a rabbit anti-NiV-nucleoprotein antibody incubated overnight (kindly
175 provided by Dr C. Broder, Uniformed Services University, Bethesda, Maryland) and a secondary
176 horseradish peroxidase (HRP)-conjugated goat antirabbit antibody (Abcam) incubated for 2 hours (both
177 1:1000). DAB substrate (ThermoScientific) was then added for 2 minutes to enable chromogenic
178 detection (brown precipitate) of HRP activity.
179
180 **RNA sequencing (RNA-seq).** Polyadenylated RNA libraries were prepared using the TruSeq RNA
181 Library Prep Kit v2 (Illumina) or TruSeq Stranded mRNA Library Prep Kit (Illumina) according to the
182 manufacturer's instructions. Libraries were sequenced on an Illumina NextSeq 500 platform using a
183 paired end 2 x 150-base pair, dual index format. Across all five marmosets (#193, #300, #340, #425, and
184 naïve) six tissue samples were sequence (lung, inguinal lymph node, kidney, gonads, brain stem, and
185 spinal cord) except gonads in the naïve marmoset. For the other five tissues in the naïve marmoset, all
186 samples were sequenced in technical duplicate. Tissues from naïve marmosets were kindly provided by
187 Dr. Ricardo Carrion Jr (Texas Biomedical Research Institute).
188
189 **RNA-seq data processing.** Trimming, alignment, and quantification were all performed in the Partek
190 Flow v10.0 [40]. Raw sequencing reads were trimmed on both edges based on quality score. Paired
191 reads were then aligned to the *Callithrix jacchus* genome (Ensemble release 91) [41] using Bowtie2
192 v2.2.5 with default parameters. Counts were generated using the Partek Quantify to Annotation Model
193 (Partek E/M) *Callithrix jacchus* annotation v105. Data normalization was performed by trimmed mean of
194 M values (TMM) adding 1.0E-4 (default parameters). Samples were filtered if the number of aligned reads
195 was less than 1 million mapped reads to genes or if they were determined to be outliers due to PCA. In
196 total, six samples were removed for the final analysis. Differential gene expression analysis was
197 performed using Partek's gene specific analysis (GSA) differential expression model.

198

199 Reads that did not map to the *Callithrix jacchus* genome were then aligned to the Nipah virus Bangladesh
200 genome (GenBank: AY988601.1) using the BWA-MEM algorithm within BWA v0.7.17 with all default
201 parameters. Transcriptional gradient and single nucleotide polymorphism analyses of the NiV_B
202 sequences was performed using IGVtools with a minimum read coverage of 100 per position and a
203 minimum variant frequency of 5%. Insert counts at the P editing site were calculated using mPileup in
204 Samtools v1.8 [42], selecting only for inserts of Gs and a minimal coverage of 100 reads per sample.

205

206 **Statistical analysis, gene set analysis, and visualization.** PCA was performed using the default
207 settings within Partek Flow v10.0. Functional enrichment analysis was performed using PantherDB's
208 Biological Processes Gene Ontology (GO) annotation set [43]. Submitted gene lists were acquired via
209 Partek's gene specific analysis (GSA) differential expression model. Lists were filtered using an FDR
210 step-up value of <0.05 and an absolute value of fold change >2. Gene lists were analyzed via the
211 PANTHER Overrepresentation Test, annotation version release data 2021-08-18. Because there are no
212 gene ontology sets for *Callithrix jacchus*, the *Homo sapiens* GO biological process complete annotation
213 data set was utilized. Only GO terms where FDR < 0.01 were used. GO terms along with accompanying
214 FDR were clustered and visualized using REVIGO [44].

Results

NiV_B infection and pathogenesis in marmosets. In the studies described here, we evaluated the susceptibility and suitability of the common marmoset to infection with NiV_B. Four marmosets were infected with NiV_B by the IN/IT routes and throughout the course of the study, survival, body weights, body temperature, blood chemistry and complete blood count (CBC) were determined (**Supplementary Figures S1, S3, and S4**). All four animals developed clinical signs of disease and reached euthanasia criteria between days 8 and 11 post infection (**Table 1**). Throughout the first seven days of the study, all subjects were normal, and only two animals (#'s 193 and 300) had loose stool on day 6 post-infection (PI). By day 8 PI, subjects #300 and #425 developed hyperventilation and did not consume their food. Subject #425 became lethargic at the end of day 8 and reached euthanasia criteria. Subject #300 started to deteriorate on day 9 PI, when found with open mouth breathing and reached euthanasia criteria the same day. Subject #193 had a reduced food consumption on days 9 and 10 PI, and on day 11 PI was found to be hyperventilating and lethargic and reached euthanasia criteria. Subject #340 was normal through day 10 PI, then developed a hunched posture, and on day 11 PI was hyperventilating and reached euthanasia criteria. Furthermore, this subject presented left hindlimb tremors during euthanasia, reflecting signs of neurological impairment. Over the course of the study, no significant changes in body weight were detected, as well as body temperature (**Supplementary Figure S1**).

X-ray autoradiography and gross pathology. To monitor development of respiratory disease, we used X-ray radiographic imaging (**Figure 1A and Supplementary Figure S2**). Over the course of the study, a decrease in normal lung tissue was observed. Prior to day 7, no radiographic changes were observed in the lungs and comparable to day 0. At day 7 PI, lungs were either still clinically normal (#193, #340), or some decreasing opacity was observed along with an appearance of an interstitial pattern (#300) and some inflammation around the smaller bronchi with a mild interstitial infiltrate (#425). At the time of euthanasia, virtually no normal lung was observed for animals #425 (euthanized day 8 PI), #300

241 (euthanized day 9 PI) and #193 (euthanized day 11 PI), as the lungs developed a nodular alveolar
242 pattern, suggesting the alveoli were filled with fluid. In animal #340 (euthanized day 11 PI), a mild
243 bronchial pattern emerged at the time of euthanasia, showing some inflammation around the smaller
244 bronchi.
245 The primary gross pathology finding identified in marmosets that reached euthanasia criteria after
246 infection with NiV_B was the presence of minimal normal lung tissues (< 5-10%) in the cranial portion of
247 the lung (**Figure 1B and Table S1**). The remaining of the lung was fluid filled with a hemorrhagic/serous
248 fluid. In one animal (#340), the right lung was normal but the bronchus fluid filled. The livers had multi-
249 focal to coalescing regions of pale circles and were very friable (**Figure 1C**). Lymph nodes (mediastinal,
250 bronchial, inguinal, and/or retropharyngeal) had gross enlargement and hemorrhage. In one animal
251 (#425), the spleen was friable and congested. Interestingly, animal #340, which presented with a less
252 severe infection of the lungs, neurological involvement was detected. An infarct was found, as well as
253 malacia near the transition zone between grey and white matter in the occipital lobe of the left cerebral
254 hemisphere. In addition, edema was present in the cerebrum. According to these observations,
255 marmosets developed diffuse pulmonary edema and hemorrhage (3 out of 4 animals), diffuse
256 hemorrhagic hepatitis (4 out of 4 animals), multi-focal hemorrhagic lymphadenopathy. One animal (#340),
257 had left ventricular cardiomyopathy and neurological complications.
258
259 **Histopathological changes in NiV_B infected marmosets.** Histopathological and immunohistochemical
260 examination of the lungs showed that all animals had mild to moderate infiltrations of mononuclear cells
261 and neutrophils in pulmonary vessels (**Figure 2A**). Subject #300 additionally showed pulmonary edema
262 with scattered presence of alveolar macrophages (data not shown). Syncytia formations were evident in
263 infected lungs (endothelial cells in pulmonary vessels or cells in alveolar septum) in all four animals. NiV
264 antigen was present in endothelial cells or smooth muscle cells of pulmonary arterioles or venules, as
265 well as in cells composing the pulmonary septa, most likely capillary endothelial cells (**Figure 2B**). In the
266 liver, all animals showed moderate to severe multifocal coagulation necroses affecting the midzonal area.

267 Mild to moderate portal inflammation with mononuclear cells and neutrophils were also evident (**Figure**
268 **2C**). Viral antigen was detected in necrotic hepatocytes and endothelial cells of the portal vein or sinusoid
269 (**Figure 2D**). In the spleens, the red pulp was partly necrotic in subject #340, while all animals retained
270 follicles without notable necrosis in white pulps. Syncytia formation was evident in mononuclear cells in
271 follicles or in red pulps (**Figure 2E**). NiV antigen was detectable in mononuclear or multinuclear syncytial
272 cells inside or surrounding follicles (**Figure 2F**). In the kidney, loss of endothelial and mesangial cells in
273 affected glomeruli was observed, along with syncytia formations of endothelial cells in the medullary
274 peritubular capillaries, cells constituting glomeruli, and the parietal epithelial cells of the Bowman's
275 capsules (**Figure 2G**). NiV nucleoprotein was detectable in glomerular endothelial cells, and peritubular
276 capillary endothelial cells (**Figure 2H**). Although there were no detectable lesions in the histopathological
277 slides, viral antigen was found in the glomerular or peritubular capillary endothelial cells in subjects #300
278 and #340. Furthermore, histopathological lesions in subject #425 suggests myocarditis associated with
279 the infiltration of mononuclear cells and neutrophils (**Figure 2I**). Viral antigen was found in the heart
280 smooth muscle cells and capillary or arteriole endothelial cells (**Figure 2J**). While no evident lesions were
281 found in the histopathological slides, viral antigen was also detected in the in heart smooth muscle cells
282 and capillary or arteriole endothelial cells of subject #300. No detectable lesions or viral antigen were
283 found in the testes (subjects #425, #193), bronchus or CNS of all subjects.
284
285 **Blood chemistry and hematology.** Over the course of the study, changes in CBC and blood chemistry
286 were monitored at days 1, 3, 5, 7, and 10 PI (**Supplementary Figures S2 and S3**). Changes over time
287 for specific parameters were compared to values obtained at day 1 PI, due to the fact that no uninfected
288 control animal was included in this study. While no change was observed in white blood cell counts for
289 subjects #300, 340, and 425, an increase at day 10 PI was measured for subject #193 one day before
290 euthanasia, indicative for leukocytosis (**Supplementary Figure S2**). Neutrophilic and eosinophilic
291 granulocytosis was noted for subjects #193, 300 and 340, and subjects #193, 300, and 425, respectively.
292 These changes were observed imminent before euthanasia. Additionally, basophilia was noted for

293 subjects #193 and 340 starting 1 DPI. No obvious changes were noted in hematocrit and platelet counts,
294 except for subject #425, for which an increase was observed at day 7 PI, one day prior to euthanasia,
295 possibly indicating reactive thrombocytosis.
296 A decreased trend in albumin levels were detected between days 1 and 5 PI for all four subjects, followed
297 by a sudden increase for animals #193 and #425 at day 7 PI, while levels for the other two subjects
298 stayed leveled. At 10 DPI a continued downward trend was observed again for the remaining two animals,
299 #193 and #340, just before euthanasia. Elevations in alkaline phosphatase at day 10 PI for subjects #193
300 and 340 were suggestive of hepatocyte damage. Similarly, a drastic increase in alanine aminotransferase
301 was noted at days 7 and 10 PI for animals #425 and 193, respectively. Amylase levels showed a
302 decreased trend over the course of the study for all four subjects, indicative for a damage in the pancreas.
303 An increase in creatinine levels was noted for subject #300 at day 7 PI and is suggestive for impaired
304 kidney function. For subject #193, a sudden decrease in creatinine levels was noted at day 10 PI, just
305 before euthanasia and could be indicative for liver damage. A temporary sudden increase in potassium
306 levels were measured for subjects #193 and 425 at day 7 PI. For animal #425, a sudden drop was
307 detected in MCH and MCHC, and an increase in RBC, and PCT at 7 DPI potentially indicating acute
308 hemorrhage. For animal #193, a temporary increase in monocytes and a drop in MCV was noted at 7
309 DPI.
310
311 **Viral titers in tissues.** Tissues were collected at time of euthanasia and viral titers determined by plaque
312 assay (**Figure 3A**). Virus was found in 19 out of 23 tissues evaluated but not consistently for the four
313 marmosets. Virus was found in the kidney and adrenals, as well as lower respiratory tract for three
314 marmosets, followed by the spleen, liver, and genitourinary system. Other tissues where virus was
315 detected in marmosets included the tonsil, upper respiratory tract, heart, gastrointestinal tract, and CNS.
316 When comparing tissues that were positive for virus between the four animals, #425 had detectable NiV_B
317 in 7 out of 10, and #300 in 6 out of the 10 tested tissue groups, while four tissues were positive for #193,
318 and one for #340. Infectious virus was found in both the brain stem and the cerebellum of #300.

319

320 **Viral RT-qPCR in tissues.** RNA was extracted from 23 tissues and RT-qPCR was performed (**Figure**
321 **3B**). Viral genome was detected in all tissues evaluated, however not for all four marmosets. Viral RNA
322 is consistently lowest for #193 but the two tissues where #193 shows the lowest Ct correspond to the
323 tissues where #193 showed the highest viral titers (liver and spleen). As expected, viral load is highest
324 across the board in tissues of the respiratory tract. Despite only one subject being positive for infectious
325 virus in the CNS, viral RNA was found in at least one of these tissues for all marmosets except #193.

326

327 **RNA-seq of NiV_B in infected marmoset tissues.** RNA was extracted from six different tissues across
328 all infected and uninfected marmosets: spinal cord, brain stem, inguinal lymph node, gonads, kidney, and
329 lung. The average tissue sample had 17.4 million reads aligned to *Callithrix jacchus*. The most highly
330 infected tissue (#425 lung) contained >180,000 virus-specific reads and 15 samples had >100 reads
331 aligned to NiV_B (**Figure 4A**). Total reads aligned to NiV_B was highly driven by overall sequencing depth,
332 however lung tissue showed the highest number of viral read counts for all animals whose lung tissue
333 sample passed quality controls.

334

335 Across all samples, reads were counted per gene, and we see that NiV in the marmoset model shows a
336 transcriptional gradient where the fraction of total reads aligned to a particular gene does not drop off
337 significantly until after N, P, and M (**Figure 4B**). In spite of the steep transcriptional gradient, three
338 samples achieved >95% coverage of L: #425 lung, #300 lung, and #300 gonads. Additionally, we were
339 able to filter all samples with >100 read coverage at the RNA editing site in P and calculate the number
340 of G inserts, with the largest number found in any individual read being 12 Gs (**Figure 4C**). Approximately
341 40% of all P-derived reads are V and W transcripts (**Figure 4D**), with proportions relatively equal but
342 varying somewhat between tissues and animals (not shown). Given the high depth of coverage we were
343 also able to identify several singe nucleotide polymorphisms (SNPs) across the NiV_B genome at rates
344 >5% of all reads when filtering for positions with a read depth > 100 reads (not shown).

345

346 **RNA-seq samples aligned to *Callithrix jacchus*.** Across all samples, an average number of 17.4 million
347 reads per sample aligned to the marmoset genome. Across all samples, we first performed differential
348 expression analysis comparing samples from NiV_B infected and uninfected animals. Only genes with an
349 FDR step up < 0.05 and an absolute value of the fold change > 2 were chose for gene ontology gene set
350 enrichment analysis. The resulting GO biological process terms were then clustered in semantic space
351 based on shared and related genes (**Figure 5A**). We see that a few clusters form with the two most
352 notable and expected dealing primarily with regulation of viral processes and interferon responses.
353 However, other clusters also emerge such as those dealing with blood circulation and angiogenesis.

354

355 We performed the same analysis on specific tissues as well, first looking at the lungs. From this we
356 identified the top 25 most significant differentially expressed genes, meeting the same filtering thresholds
357 described previously. We then visualized the differential expression using a hierarchically clustered
358 heatmap (**Figure 5B**). Here we see expected interferon stimulated genes such as ISG15, ISG20, OAS3,
359 OASL, and IFNB1 upregulated in infected tissues. However, we see only a single gene downregulated
360 relative to the naïve samples make the top 25 cutoff: SCGB3A2. Secretoglobin (SCGB) 3A2 is known to
361 have anti-inflammatory properties, especially in allergic airway inflammation models [45] although its role
362 in viral infections has not been previously shown.

363

364 We also performed principal component analysis of brain stem samples from infected and uninfected
365 animals (**Figure 5C**). One sample stands as a clear outlier, the brain stem from marmoset #340, the only
366 marmoset to have shown overt neurologic clinical symptoms (blue sphere). Due to the unique clinical
367 symptoms and the results of the PCA we performed differential expression analysis comparing the brain
368 stem sample from #340 to the other three infected brain stem samples (#193, #300, and #425). Filtering
369 genes using the same thresholds as above, then extracting enriched GO biological process terms, and
370 mapping the interconnectedness of the resulting GO terms, we found a large, interconnected graph of

371 unique and related terms (**Figure 5D**). The largest interconnected tree graph shows a family of GO terms
372 relating to myelination, oligodendrocyte development, and glial cell development. These results are
373 noteworthy given previous findings of significant myelin degradation and axonal NiV aggregation in
374 hamsters infected with NiV_M [46].

375 **Discussion**

376

377 In this study we identify marmosets as a highly susceptible novel new-world NHP model of NiV_B infection.
378 Four marmosets, two male and two female, were infected with NiV_B via the IN/IT routes and all four
379 animals succumbed to infection by day 11 PI. The marmosets recapitulated many of the same clinical
380 symptoms seen in patients and other NHP models infected with NiV, such as anorexia, lethargy, and
381 hyperventilation. Of special note, one marmoset, subject #340, presented with left hindlimb tremors on
382 day 11 PI, displaying overt neurological clinical symptoms. In the setting of acute infection with NiV_B,
383 neurological clinical symptoms are rare [34] although neurological disease seen on MRI, in
384 histopathology, or in gross pathology is relatively common [22,24,27,31,33]. However, in infections with
385 NiV_M, neurological clinical symptoms are more common, especially among NHPs surviving longer
386 [21,28,29]. This may give some insight into the development of neurological clinical symptoms in the only
387 marmoset (#340) that presented a less severe infection of the lungs, with all other animals having <5-
388 10% normal lung tissue following euthanasia. #340 was found to have a cerebral infarct, malacia in the
389 occipital lobe of the left cerebral hemisphere, and cerebral edema. This animal, uniquely, also displayed
390 left ventricular cardiomyopathy.

391

392 On histopathological examination, all marmosets were found to have significant multifocal coagulation in
393 the liver, syncytia formation of endothelial cells in the kidney, and infiltration in the lung.
394 Immunohistochemistry showed NiV antigen in syncytial cells across multiple tissues, notably in the
395 smooth muscle cells and capillary endothelial cells of the heart. No detectable viral antigen was found in
396 the CNS of all subjects. Blood chemistry and hematology showed consistent hypoalbuminemia across
397 all animals, reactive thrombocytosis in marmoset #425, decreases in amylase indicating pancreatic
398 damage across all marmosets, and increased creatinine in subject #300 indicating impaired kidney
399 function. These findings replicate the clinical and pathophysiological picture of NiV infection in NHPs.

400 Especially importantly is the finding not only of neurological disease, but a marmoset with neurological
401 clinical symptoms following NiV_B infection.
402
403 Viral titers were performed showing titerable virus from all tissue sets evaluated, but some variance was
404 seen across subjects. Infectious virus was also tittered from both the brain stem and cerebellum of #300.
405 Performing RT-qPCR showed that viral RNA was detectable in all tissues tested but not in all marmosets.
406 Viral RNA was most prevalent in the lower respiratory tract, as expected, but was also found in at least
407 one tissue each within the CNS for #300, 340, and 425.
408
409 RNA-seq was performed providing deeper insight into both the NiV and marmoset transcriptional patterns
410 across multiple tissues. The number of reads aligned to the *Callithrix* jacchus genome was high across
411 all tissues, but the number of reads aligning to NiV_B was highly variable. More highly infected tissues,
412 especially the lungs, tended to have the highest number and proportion of NiV reads. Additionally, RNA-
413 seq of NiV_B showed a transcriptional gradient that did not drop significantly until after matrix, a pattern
414 not typically seen among other viruses of the family *Paramyxoviridae* [47,48]. We also showed that RNA
415 editing of P results in very similar amounts of W and V, in contrast to the steep drop from P often seen in
416 other paramyxoviruses [49,50]. However, others have shown this same pattern in NiV_B with
417 approximately 40-50% of reads being P while the remaining reads are nearly evenly split between V and
418 W [51]. Similarly, we replicated *in vivo* the findings that the number of G additions is nearly flat from +1
419 to +5 as seen in 293 cells [51].
420
421 By looking at the marmoset transcriptome, across all tissues we observed a consistent up-regulation of
422 gene ontologies relating to regulation of viral processes and interferon stimulated genes. We found
423 results mirroring those found in AGMs showing especially significant upregulation of genes such as *MX2,*
424 *OASL, CCL2*, and *ISG15* in the most highly infected tissue, the lung. When evaluating the tissue-specific
425 transcriptomic responses to infection, the principal component analysis of brain stem samples showed

426 that #340 was a significant outlier relative to all other samples. When exploring the differential expression
427 in the sample from #340 we found a particular enrichment in genes relating to myelination, axon
428 ensheathment, and oligodendrocytes relative to other infected marmosets. Previous findings of myelin
429 degradation and axonal NiV antigen aggregation in hamsters may be related findings to what we observe
430 here in marmosets [46].
431
432 Marmosets may provide a new NHP model to study severe respiratory disease caused by NiV. These
433 findings are of particular note given many of the logistical advantages afforded by working with
434 marmosets in the context of high-biocontainment human respiratory pathogens like NiV. Marmosets offer
435 distinct advantages to the current standard NHP model of NiV infection, AGMs, due to their small size
436 and ease of handling, typically lower costs, and ease of co-housing allowing for a potential model of
437 transmission studies. Given the unique transcriptional profile in the brain stem of the only marmoset that
438 showed neurologic clinical symptoms, there is a need for additional follow up with a larger cohort number
439 of both infected and uninfected marmosets. More detailed pathogenicity studies are required to monitor
440 levels of viremia during the course of disease development, as well as evaluate different routes of
441 infection to potentially allow in depth studying of neuroinvasion. Overall, marmosets were highly
442 susceptible to infection via the IN/IT route resulting in a 100% mortality in non-protected animals.

443

444 **References**

445

446 1. Looi L-M, Chua K-B. Lessons from the Nipah virus outbreak in Malaysia. Malays J Pathol
447 [Internet]. **2007**; 29(2):63–7. Available from: http://www.ncbi.nlm.nih.gov/pubmed/19108397

448 2. Howley PM, Knipe DM (David M, Whelan SPJ, Fields BN. Fields virology. Volume 1, Emerging
449 viruses . Seventh ed. Philadelphia, PA: Lippincott Williams & Wilkins; 2021.

450 3. Goh KJ, Tan CT, Chew NK, et al. Clinical Features of Nipah Virus Encephalitis among Pig
451 Farmers in Malaysia. N Engl J Med [Internet]. Massachusetts Medical Society; **2000**;
452 342(17):1229–1235. Available from: https://doi.org/10.1056/NEJM200004273421701

453 4. Hossain MJ, Gurley ES, Montgomery JM, et al. Clinical presentation of nipah virus infection in
454 Bangladesh. Clin Infect Dis an Off Publ Infect Dis Soc Am. United States; **2008**; 46(7):977–984.

455 5. Chadha MS, Comer JA, Lowe L, et al. Nipah Virus-associated Encephalitis Outbreak, Siliguri,
456 India. Emerg Infect Dis [Internet]. **2006**; 12(2):235–240. Available from:
457 http://wwwnc.cdc.gov/eid/article/12/2/05-1247_article.htm

458 6. Homaira N, Rahman M, Hossain MJ, et al. Nipah virus outbreak with person-to-person
459 transmission in a district of Bangladesh, 2007. Epidemiol Infect [Internet]. **2010**; 138(11):1630–
460 1636. Available from:
461 https://www.cambridge.org/core/product/identifier/S0950268810000695/type/journal_article

462 7. Mungall BA, Middleton D, Crameri G, et al. Vertical Transmission and Fetal Replication of Nipah
463 Virus in an Experimentally Infected Cat. J Infect Dis [Internet]. **2007**; 196(6):812–816. Available

464 from: https://academic.oup.com/jid/article-lookup/doi/10.1086/520818

465 8. McEachern JA, Bingham J, Crameri G, et al. A recombinant subunit vaccine formulation protects
466 against lethal Nipah virus challenge in cats. Vaccine [Internet]. **2008**; 26(31):3842–3852.
467 Available from: https://linkinghub.elsevier.com/retrieve/pii/S0264410X08005720

468 9. Dups J, Middleton D, Long F, Arkinstall R, Marsh GA, Wang L-F. Subclinical infection without
469 encephalitis in mice following intranasal exposure to Nipah virus-Malaysia and Nipah virus-
470 Bangladesh. Virol J [Internet]. **2014**; 11(1):102. Available from:
471 https://virologyj.biomedcentral.com/articles/10.1186/1743-422X-11-102

472 10. Valbuena G, Halliday H, Borisevich V, Goez Y, Rockx B. A Human Lung Xenograft Mouse Model
473 of Nipah Virus Infection. Pekosz A, editor. PLoS Pathog [Internet]. **2014**; 10(4):e1004063.
474 Available from: https://dx.plos.org/10.1371/journal.ppat.1004063

475 11. Kasloff SB, Leung A, Pickering BS, et al. Pathogenicity of Nipah henipavirus Bangladesh in a
476 swine host. Sci Rep [Internet]. **2019**; 9(1):5230. Available from:
477 http://www.nature.com/articles/s41598-019-40476-y

478 12. Torres-Velez FJ, Shieh W-J, Rollin PE, et al. Histopathologic and Immunohistochemical
479 Characterization of Nipah Virus Infection in the Guinea Pig. Vet Pathol [Internet]. **2008**;
480 45(4):576–585. Available from: http://journals.sagepub.com/doi/10.1354/vp.45-4-576

481 13. Clayton BA, Middleton D, Bergfeld J, et al. Transmission Routes for Nipah Virus from Malaysia
482 and Bangladesh. Emerg Infect Dis [Internet]. **2012**; 18(12):1983–1993. Available from:
483 http://wwwnc.cdc.gov/eid/article/18/12/12-0875_article.htm

484 14. Satterfield BA, Cross RW, Fenton KA, et al. The immunomodulating V and W proteins of Nipah
485 virus determine disease course. Nat Commun [Internet]. **2015**; 6(1):7483. Available from:
486 http://www.nature.com/articles/ncomms8483

487 15. Bossart KN, Zhu Z, Middleton D, et al. A Neutralizing Human Monoclonal Antibody Protects
488 against Lethal Disease in a New Ferret Model of Acute Nipah Virus Infection. Basler CF, editor.
489 PLoS Pathog [Internet]. **2009**; 5(10):e1000642. Available from:
490 https://dx.plos.org/10.1371/journal.ppat.1000642

491 16. Wong KT, Grosjean I, Brisson C, et al. A Golden Hamster Model for Human Acute Nipah Virus
492 Infection. Am J Pathol [Internet]. **2003**; 163(5):2127–2137. Available from:
493 https://linkinghub.elsevier.com/retrieve/pii/S0002944010635699

494 17. Weingartl H, Czub S, Copps J, et al. Invasion of the Central Nervous System in a Porcine Host
495 by Nipah Virus. J Virol [Internet]. **2005**; 79(12):7528–7534. Available from:
496 https://journals.asm.org/doi/10.1128/JVI.79.12.7528-7534.2005

497 18. Middleton DJ, Westbury HA, Morrissy CJ, et al. Experimental Nipah Virus Infection in Pigs and
498 Cats. J Comp Pathol [Internet]. **2002**; 126(2–3):124–136. Available from:
499 https://linkinghub.elsevier.com/retrieve/pii/S0021997501905328

500 19. Dhondt KP, Mathieu C, Chalons M, et al. Type I Interferon Signaling Protects Mice From Lethal
501 Henipavirus Infection. J Infect Dis [Internet]. **2013**; 207(1):142–151. Available from:
502 https://academic.oup.com/jid/article-lookup/doi/10.1093/infdis/jis653

503 20. Geisbert TW, Daddario-DiCaprio KM, Hickey AC, et al. Development of an Acute and Highly
504 Pathogenic Nonhuman Primate Model of Nipah Virus Infection. Jacobson S, editor. PLoS One

505 [Internet]. **2010**; 5(5):e10690. Available from: https://dx.plos.org/10.1371/journal.pone.0010690

506 21. Johnston SC, Briese T, Bell TM, et al. Detailed Analysis of the African Green Monkey Model of
507 Nipah Virus Disease. Elankumaran S, editor. PLoS One [Internet]. **2015**; 10(2):e0117817.
508 Available from: https://dx.plos.org/10.1371/journal.pone.0117817

509 22. Prasad AN, Agans KN, Sivasubramani SK, et al. A Lethal Aerosol Exposure Model of Nipah
510 Virus Strain Bangladesh in African Green Monkeys. J Infect Dis [Internet]. **2020**;
511 221(Supplement_4):S431–S435. Available from:
512 https://academic.oup.com/jid/article/221/Supplement_4/S431/5610171

513 23. Lo MK, Feldmann F, Gary JM, et al. Remdesivir (GS-5734) protects African green monkeys from
514 Nipah virus challenge. Sci Transl Med [Internet]. **2019**; 11(494):eaau9242. Available from:
515 https://stm.sciencemag.org/lookup/doi/10.1126/scitranslmed.aau9242

516 24. Mire CE, Geisbert JB, Agans KN, et al. Use of Single-Injection Recombinant Vesicular Stomatitis
517 Virus Vaccine to Protect Nonhuman Primates Against Lethal Nipah Virus Disease. Emerg Infect
518 Dis [Internet]. **2019**; 25(6):1144–1152. Available from: http://wwwnc.cdc.gov/eid/article/25/6/18-
519 1620_article.htm

520 25. Prasad AN, Woolsey C, Geisbert JB, et al. Resistance of Cynomolgus Monkeys to Nipah and
521 Hendra Virus Disease Is Associated With Cell-Mediated and Humoral Immunity. J Infect Dis
522 [Internet]. **2020**; 221(Supplement_4):S436–S447. Available from:
523 https://academic.oup.com/jid/article/221/Supplement_4/S436/5727782

524 26. Geisbert TW, Mire CE, Geisbert JB, et al. Therapeutic Treatment of Nipah Virus Infection in
525 Nonhuman Primates with a Neutralizing Human Monoclonal Antibody. Sci Transl Med [Internet].

526 **2014**; 6(242):242ra82-242ra82. Available from:
527 https://stm.sciencemag.org/lookup/doi/10.1126/scitranslmed.3008929

528 27. Geisbert JB, Borisevich V, Prasad AN, et al. An Intranasal Exposure Model of Lethal Nipah Virus
529 Infection in African Green Monkeys. J Infect Dis [Internet]. **2020**; 221(Supplement_4):S414–
530 S418. Available from: https://academic.oup.com/jid/article/221/Supplement_4/S414/5610161

531 28. Liu J, Coffin KM, Johnston SC, et al. Nipah virus persists in the brains of nonhuman primate
532 survivors. JCI Insight [Internet]. **2019**; 4(14). Available from:
533 https://insight.jci.org/articles/view/129629

534 29. Lee JH, Hammoud DA, Cong Y, et al. The Use of Large-Particle Aerosol Exposure to Nipah
535 Virus to Mimic Human Neurological Disease Manifestations in the African Green Monkey. J
536 Infect Dis [Internet]. **2020**; 221(Supplement_4):S419–S430. Available from:
537 https://academic.oup.com/jid/article/221/Supplement_4/S419/5613084

538 30. Lara A, Cong Y, Jahrling PB, et al. Peripheral immune response in the African green monkey
539 model following Nipah-Malaysia virus exposure by intermediate-size particle aerosol. Geisbert T,
540 editor. PLoS Negl Trop Dis [Internet]. **2019**; 13(6):e0007454. Available from:
541 https://dx.plos.org/10.1371/journal.pntd.0007454

542 31. Cong Y, Lentz MR, Lara A, et al. Loss in lung volume and changes in the immune response
543 demonstrate disease progression in African green monkeys infected by small-particle aerosol
544 and intratracheal exposure to Nipah virus. Horby P, editor. PLoS Negl Trop Dis [Internet]. **2017**;
545 11(4):e0005532. Available from: https://dx.plos.org/10.1371/journal.pntd.0005532

546 32. Marianneau P, Guillaume V, Wong KT, et al. Experimental Infection of Squirrel Monkeys with

547 Nipah Virus. Emerg Infect Dis [Internet]. **2010**; 16(3):507–510. Available from:
548 http://wwwnc.cdc.gov/eid/article/16/3/09-1346_article.htm

549 33. Hammoud DA, Lentz MR, Lara A, et al. Aerosol exposure to intermediate size Nipah virus
550 particles induces neurological disease in African green monkeys. Bente DA, editor. PLoS Negl
551 Trop Dis [Internet]. **2018**; 12(11):e0006978. Available from:
552 https://dx.plos.org/10.1371/journal.pntd.0006978

553 34. Mire CE, Satterfield BA, Geisbert JB, et al. Pathogenic Differences between Nipah Virus
554 Bangladesh and Malaysia Strains in Primates: Implications for Antibody Therapy. Sci Rep
555 [Internet]. **2016**; 6(1):30916. Available from: http://www.nature.com/articles/srep30916

556 35. Gómez Román R, Wang L-F, Lee B, et al. Nipah@20: Lessons Learned from Another Virus with
557 Pandemic Potential. Imperiale MJ, editor. mSphere [Internet]. **2020**; 5(4). Available from:
558 https://journals.asm.org/doi/10.1128/mSphere.00602-20

559 36. Pelissier R, Iampietro M, Horvat B. Recent advances in the understanding of Nipah virus
560 immunopathogenesis and anti-viral approaches. F1000Research [Internet]. **2019**; 8:1763.
561 Available from: https://f1000research.com/articles/8-1763/v1

562 37. Worley KC, Warren WC, Rogers J, et al. The common marmoset genome provides insight into
563 primate biology and evolution. Nat Genet [Internet]. **2014**; 46(8):850–857. Available from:
564 https://doi.org/10.1038/ng.3042

565 38. Okano H, Hikishima K, Iriki A, Sasaki E. The common marmoset as a novel animal model
566 system for biomedical and neuroscience research applications. Semin Fetal Neonatal Med
567 [Internet]. **2012**; 17(6):336–340. Available from:

568 https://linkinghub.elsevier.com/retrieve/pii/S1744165X12000844

569 39. Yun T, Park A, Hill TE, et al. Efficient Reverse Genetics Reveals Genetic Determinants of
570 Budding and Fusogenic Differences between Nipah and Hendra Viruses and Enables Real-Time
571 Monitoring of Viral Spread in Small Animal Models of Henipavirus Infection. J Virol [Internet].
572 American Society for Microbiology; **2021**; 89(2):1242–1253. Available from:
573 https://doi.org/10.1128/JVI.02583-14

574 40. Partek Inc. Partek® Flow® (Version 10.0). 2020.

575 41. Howe KL, Achuthan P, Allen J, et al. Ensembl 2021. Nucleic Acids Res [Internet]. **2021**;
576 49(D1):D884–D891. Available from: https://academic.oup.com/nar/article/49/D1/D884/5952199

577 42. Danecek P, Bonfield JK, Liddle J, et al. Twelve years of SAMtools and BCFtools. Gigascience
578 [Internet]. **2021**; 10(2). Available from:
579 https://academic.oup.com/gigascience/article/doi/10.1093/gigascience/giab008/6137722

580 43. Thomas PD, Kejariwal A, Guo N, et al. Applications for protein sequence-function evolution data:
581 mRNA/protein expression analysis and coding SNP scoring tools. Nucleic Acids Res [Internet].
582 **2006**; 34(Web Server):W645–W650. Available from: https://academic.oup.com/nar/article-
583 lookup/doi/10.1093/nar/gkl229

584 44. Supek F, Bošnjak M, Škunca N, Šmuc T. REVIGO Summarizes and Visualizes Long Lists of
585 Gene Ontology Terms. Gibas C, editor. PLoS One [Internet]. **2011**; 6(7):e21800. Available from:
586 https://dx.plos.org/10.1371/journal.pone.0021800

587 45. Yoneda M, Xu L, Kajiyama H, et al. Secretoglobin Superfamily Protein SCGB3A2 Alleviates

588 House Dust Mite-Induced Allergic Airway Inflammation in Mice. Int Arch Allergy Immunol
589 [Internet]. **2016**; 171(1):36–44. Available from: https://www.karger.com/Article/FullText/450788

590 46. Munster VJ, Prescott JB, Bushmaker T, et al. Rapid Nipah virus entry into the central nervous
591 system of hamsters via the olfactory route. Sci Rep [Internet]. **2012**; 2(1):736. Available from:
592 http://www.nature.com/articles/srep00736

593 47. Wignall-Fleming EB, Hughes DJ, Vattipally S, et al. Analysis of Paramyxovirus Transcription and
594 Replication by High-Throughput Sequencing. Dutch RE, editor. J Virol [Internet]. **2019**; 93(17).
595 Available from: https://journals.asm.org/doi/10.1128/JVI.00571-19

596 48. Cox RM, Krumm SA, Thakkar VD, Sohn M, Plemper RK. The structurally disordered
597 paramyxovirus nucleocapsid protein tail domain is a regulator of the mRNA transcription
598 gradient. Sci Adv [Internet]. **2017**; 3(2). Available from:
599 https://www.science.org/doi/10.1126/sciadv.1602350

600 49. Cox R, Plemper RK. The paramyxovirus polymerase complex as a target for next-generation
601 anti-paramyxovirus therapeutics. Front Microbiol [Internet]. **2015**; 6. Available from:
602 http://www.frontiersin.org/Virology/10.3389/fmicb.2015.00459/abstract

603 50. Rao PL, Gandham RK, Subbiah M. Molecular evolution and genetic variations of V and W
604 proteins derived by RNA editing in Avian Paramyxoviruses. Sci Rep [Internet]. **2020**; 10(1):9532.
605 Available from: http://www.nature.com/articles/s41598-020-66252-x

606 51. Lo MK, Harcourt BH, Mungall BA, et al. Determination of the henipavirus phosphoprotein gene
607 mRNA editing frequencies and detection of the C, V and W proteins of Nipah virus in virus-
608 infected cells. J Gen Virol [Internet]. **2009**; 90(2):398–404. Available from:

https://www.microbiologyresearch.org/content/journal/jgv/10.1099/vir.0.007294-0

611 **Figure Legends**

612 **Table 1. Clinical description and diagnosis in NiV_B infected marmosets.**

613 Graphical representation of clinical descriptions and diagnoses of all four marmosets infected with NiV_B.

614 Further detail is available in **Table S1**.

615

616 **Figure 1: Progressive pathogenesis in marmosets after NiV_B infection.**

617 **(A)** Subject #300 was positioned in a ventral dorsal position and all images are in a R -> L orientation.

618 X-ray images of the chest were taken on days 0, 1, 3, 5, 7, and at euthanasia. Prior to day 7, lungs

619 appeared normal. Progressive lung pathology was detected from day 7 onward, with a decrease in

620 normal lung tissue over the experimental infection course. By day 7, some decreasing opacity was

621 observed along with an appearance of an interstitial pattern. At the time of Euthanasia (day 9 post-

622 infection), virtually no normal lung was observed as the lungs develop a nodular alveolar pattern,

623 suggesting the alveoli are filled with fluid. **(B)** Lung of subject #425 at time of euthanasia at day 8 post-

624 infection. Acute diffuse pulmonary hemorrhage, with hemorrhage involving all lobes and <10% of

625 normal tissue remaining. **(C)** Liver of subject #425. Diffuse massive necrosis of the liver, with necrosis

626 involving all lobes and normal structure visible.

627

628 **Figure 2: Histopathological changes in marmoset tissues after NiV_B infection.**

629 **Panels A, C, E, G, I:** H&E staining. **Panels B, D, F, H, J:** Immunohistochemical staining for NiV

630 nucleoprotein.

631 **(A)** Lung (subject #340): Mild to moderate infiltration of mononuclear cells (macrophages, monocytes)

632 and neutrophils in perivascular space. **(B)** Lung (subject #425): NiV antigen present in endothelial cells

633 and smooth muscle cells of pulmonary vessels (arteriole, venule). **(C)** Liver (subject 340): Focal

634 coagulation necrosis in midzonal hepatocytes, surrounded by inflammatory cells (neutrophils,

635 mononuclear cells). **(D)** Liver (subject #425): NiV antigen present in hepatocytes, sinusoidal endothelial

636 cells, and portal vein endothelial cells. **(E)** Spleen (subject #340): Necrosis of red pulp and formation of
637 syncytial cells. **(F)** Spleen (subject #425): NiV antigen present in mononuclear or multinuclear cells in
638 peripheral zone of follicles, or in red pulp. **(G)** Kidney (subject #300): Loss of endothelial and mesangial
639 cells in affected glomeruli. **(H)** Kidney (subject #425): NiV antigen present in glomerular cells and
640 peritubular capillary endothelial cells. **(I)** Heart (subject #425): Mild myocarditis with necrosis of
641 myocytes and infiltration of mononuclear cells and neutrophils. **(J)** Heart (subject #425): NiV antigen
642 present in capillary and arteriole endothelial cells, as well as heart muscle cells.
643
644 **Figure 3. Viral titers and viral RT-qPCR data across various tissues.**
645 **(A)** At time of euthanasia, tissues were collected. Viral titers were determined by plaque assay in 23
646 tissues, combined into 10 tissues systems seen here. Values equal to zero were set to 10^0 for
647 visualization on a log-scale. Tissue systems with more than one tissue type are upper respiratory tract
648 (nasal mucosa and trachea), lower respiratory tract (left upper lobe, left lower lobe, right upper lobe,
649 and right lower lobe of the lung as well as each of the left and right bronchi), kidney and adrenals
650 (kidney and adrenal gland), gastrointestinal tract (pancreas, jujunum, and colon transversum), central
651 nervous system (brain-frontal, brain-cerebellum, brain stem, and cervical spinal cord), and genitourinary
652 system (urinary bladder and gonads). **(B)** RT-qPCR was performed to determine relative amounts of
653 viral RNA across 23 tissues. Average cycle threshold for uninfected samples is shown (dotted line).
654 Alternating white and gray fill for box and whisker plots separate similar tissue types (e.g. all lymph
655 node (LN) samples are adjacent and grey). Both right (R) and left (L) lower and upper lung samples are
656 also shown adjacent and with the same fill color (grey).
657
658 **Figure 4. RNA-seq of NiV_B in infected marmoset tissues.**
659 **(A)** Total number of reads aligned to *Callithrix jacchus* (cyan) and NiV_B (dark blue) are shown across all
660 tissues and samples. The dotted line indicates 100 aligned reads, the threshold for inclusion into 4B.
661 **(B)** The fraction of total NiV_B aligned reads corresponding to each Nipah virus gene across all samples

662 meeting the 100 read threshold. **(C)** The fraction of reads with the indicated number of inserted
663 guanines (Gs) at the RNA editing site in P for all samples meeting the threshold of 100 reads aligned to
664 the RNA editing site. **(D)** The fraction reads at the P editing site resulting in P, V, or W based on the
665 number of inserted Gs.
666
667 **Figure 5. RNA-seq samples aligned to *Callithrix jacchus*.**
668 For all subfigures, differential expressed genes must meet the threshold of FDR step up < 0.0 and,
669 absolute value of fold change > 2. **(A)** Across all animals and all tissues, differential expression analysis
670 was performed comparing infected and uninfected samples. Filtered differentially expressed genes
671 were used to obtain enriched gene ontology (GO) gene sets, and similar terms were clustered.
672 Log_{10}(FDR) of the gene set is indicated by the color and log_{10} of the number of terms in the gene set is
673 indicated by the size of the circle. **(B)** Differential expression analysis only in the lung samples across
674 all animals were used to identify the top 25 differentially expressed genes and then hierarchical
675 clustering was performed to obtain a heatmap. Genes in red are more expressed relative to the other
676 samples and genes in blue are less expressed. **(C)** Principal component analysis was performed on the
677 brain stem samples across all animals. The top three principal components are shown. Tissues from
678 infected animals (blue) and tissues from uninfected animals (red) are further broken down into tissues
679 from animals showing clinical neurological signs (sphere). This was only seen in marmoset #340. **(D)**
680 The top differentially expressed genes between #340 and the other animals were used to ascertain
681 enriched GO terms. The largest interconnected family of GO terms is shown with darker red indicating
682 a lower FDR and a larger circle indicating more genes in a particular GO term.
683

684 **Supplementary Figure Legends**

685

686 **Table S1. Clinical description and diagnosis in NiV_B infected marmosets.**

687 Detailed descriptions of clinical and gross pathology as well as clinical diagnoses for all four marmosets

688 infected with NiV_B.

689

690 **Figure S1: Changes in body weight and temperature in marmosets after NiV_B infection.**

691 (A) Changes in body weight are shown as percent change compared to the individual starting weight at

692 day 0 of the study. (B) Changes in body temperature are shown as changes in ºF compared to the first

693 measurement made on day 1 post-infection. Subject #193 is shown in orange circles, subject #300 in

694 red circles, subject #340 in green circles, and subject #425 in blue circles.

695

696 **Figure S2: Progressive lung pathogenesis in marmosets after NiV_B infection.**

697 Subject were positioned in a left lateral position and all images are in a Cranial to Caudal orientation. X-

698 ray images were taken on days 0, 1, 3, 5, 7, and at euthanasia. Prior to day 7, lungs appeared normal.

699 Progressive lung pathology was detected from day 7 onward. **(A)** Subject #340: A mild bronchial

700 pattern emerged at the time of euthanasia (day 9 post-infection) and showed some inflammation

701 around the smaller bronchi, compared to day 7. **(B)** Subject #425: A severe interstitial pattern with

702 nodules emerged at the time of euthanasia (day 11 post-infection), compared to day 7 where the

703 animal was showing some inflammation around the smaller bronchi with a mild interstitial infiltrate. **(C)**

704 Subject #193: A severe interstitial pattern emerged at the time of euthanasia (day 11 post-infection),

705 compared to day 7 where the lung was completely normal

706

707 **Supplementary Figure S3. Changes in complete blood count.**

708 Taken at days 1, 3, 5, 7, and 10, hematological analysis included total white blood cell counts, white

709 blood cell differential, red blood cell counts, platelet counts, hematocrit values, total hemoglobin

710 concentrations, mean cell volumes, mean corpuscular volumes and mean corpuscular hemoglobin
711 concentrations. White blood cell count (WBC), neutrophils (Neu), eosinophils (Eos), basophils (Bas),
712 hematocrit (HCT), and platelets (PLT.
713
714 **Supplementary Figure S4. Changes in blood chemistry.**
715 Clinical chemistry analysis was performed at days 1, 3, 5, 7, and 10. Serum samples were tested for
716 concentrations of albumin, alanine aminotransferase (ALT), alkaline phosphatase (ALP), glucose,
717 plasma electrolytes (blood urea nitrogen (BUN) and creatinine (CRE)).
718
719 **Supplementary Figure S5. Additional changes in complete blood count.**
720 Taken at days 1, 3, 5, 7, and 10, hematological analysis included total white blood cell counts, white
721 blood cell differential, red blood cell counts, platelet counts, hematocrit values, total hemoglobin
722 concentrations, mean cell volumes, mean corpuscular volumes and mean corpuscular hemoglobin
723 concentrations. Red blood cell count (RBC), lymphocytes (LYM), monocytes (Mon), plateletcrit (PCT),
724 platelet distribution width (PDWs), platelet distribution width % (PDWc), hemoglobin (HGB), mean
725 corpuscular volume (MCV), mean corpuscular hemoglobin (MCH), mean corpuscular hemoglobin
726 concentration (MCHC), red cell distribution width (RDWs), red cell distribution width % (RDWc), and
727 mean platelet volume (MPV).
728
729 **Supplementary Figure S6. Additional changes in blood chemistry.**
730 Clinical chemistry analysis was performed at days 1, 3, 5, 7, and 10. Serum samples were tested for
731 concentrations of amylase (AMY), total protein (TP), total bilirubin (TBIL), plasma electrolytes (calcium
732 (CA), phosphorus (Phos), sodium (Na+), and potassium (K+), and globulin (GLOB)).

Nipah virus Bangladesh infection elicits organ-specific innate and inflammatory responses in the marmoset model

Christian S. Stevens[1], Jake Lowry[2], Terry Juelich[3], Colm Atkins[3,#], Kendra Johnson[4], Jennifer K Smith[3], Maryline Panis[1], Tetsuro Ikegami[3], Benjamin tenOever[1], Alexander N. Freiberg[3], Benhur Lee[1]

[1]Icahn School of Medicine at Mount Sinai, Department of Microbiology

[2]University of Texas Medical Branch, Animal Resource Center

[3]University of Texas Medical Branch, Department of Pathology

[4]University of Texas Medical Branch, Department of Microbiology and Immunology

[#]Present address: Rutgers University, Department of Cell Biology and Neuroscience

Table 1. Clinical description and diagnosis in NiV_B infected marmosets

	Clincal Diagnosis	193 Male 11 DPI	300 Female 9 DPI	340 Female 11 DPI	425 Male 8 DPI
(1)	Diffuse Pulmonary Edema and Hemorrhage	✅	✅	✅	✅
(2)	Diffuse hemorrhagic hepatitis	✅	✅	✅	✅
(3)	Multi-focal hemorrhagic Lymphadenopathy	✅	✅		✅
(4)	Hemorrhagic Tonsilitis		✅		
(5)	Splenic Congestion				✅
(6)	Left Ventricular Cardiomyopathy / Right Atrial Dilation			✅	
(7)	Cerebral Infarct and malacia in the occipital lobe			✅	
(8)	Cerebral Edema			✅	
	(Left Hindlimb tremors at euthansia)			✅	

Figure 1. X-ray autoradiography and gross pathology.

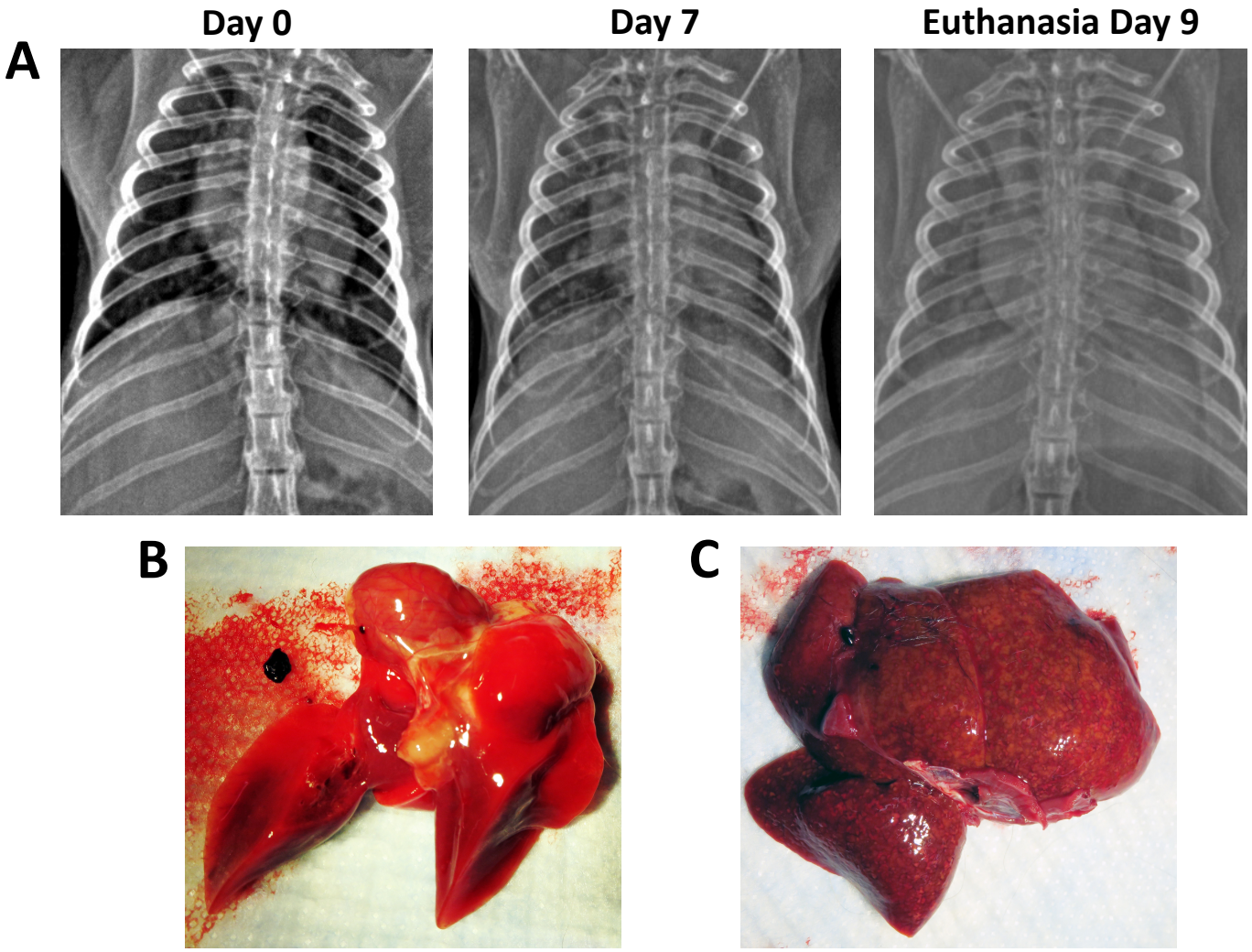

Figure 2. Histopathological changes in NiV_B infected marmosets.

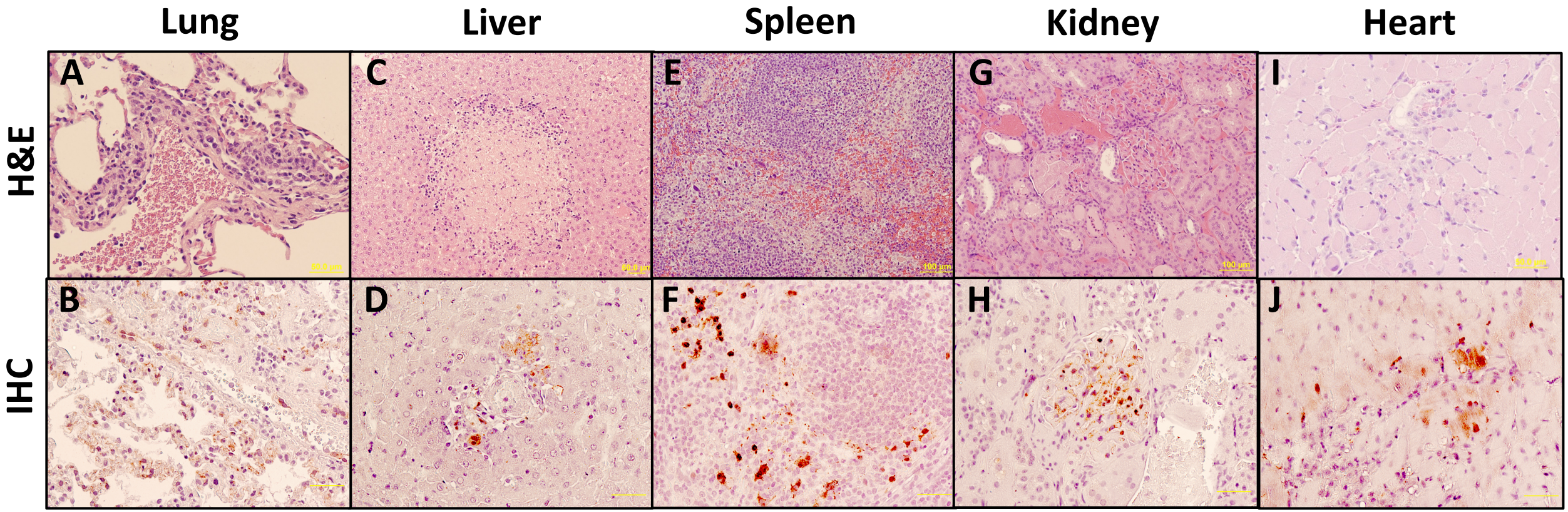

Figure 3. Viral titers and viral RT-qPCR data.

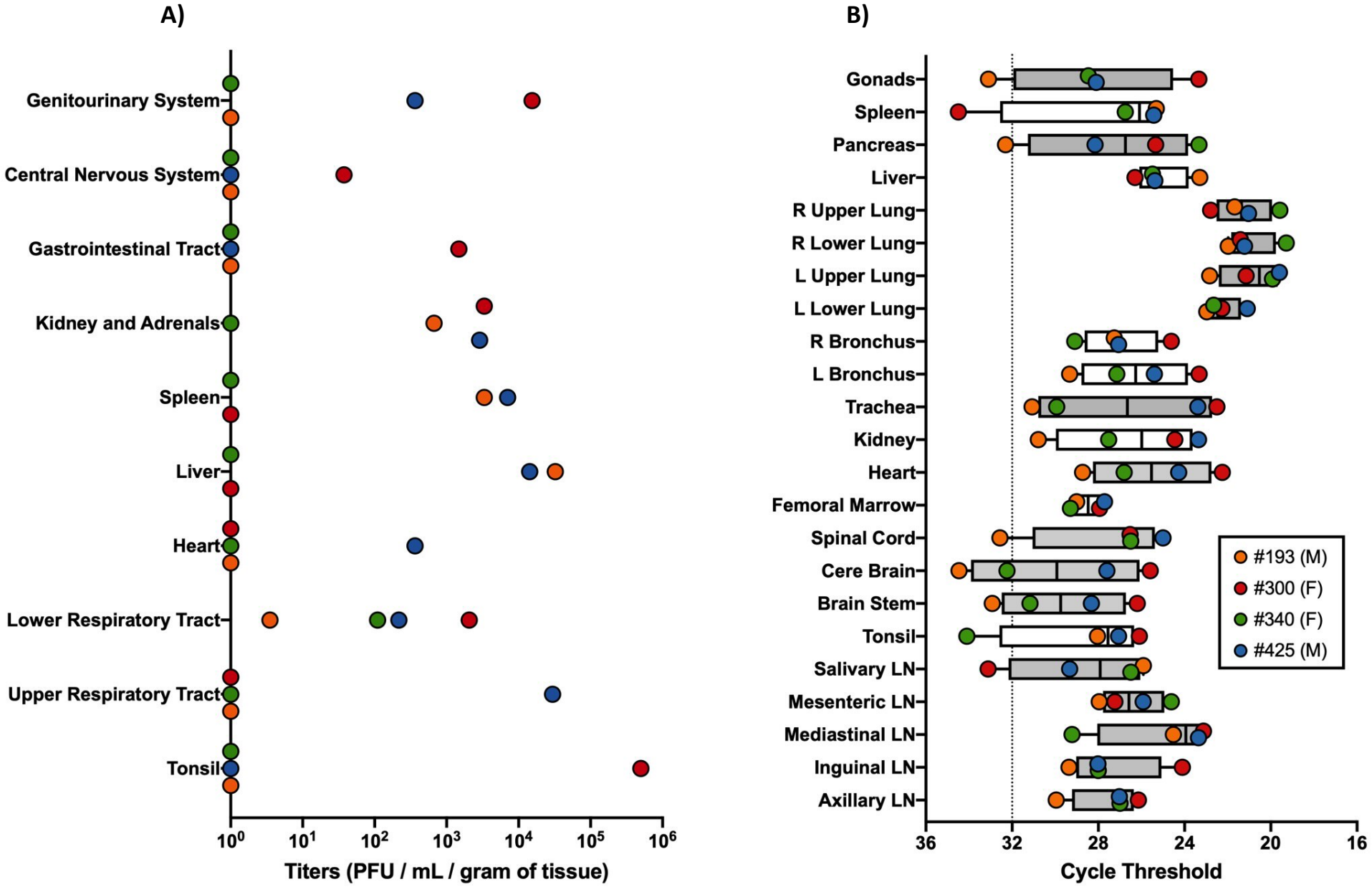

Figure 4. RNA-seq of NiV_B in infected marmoset tissues.

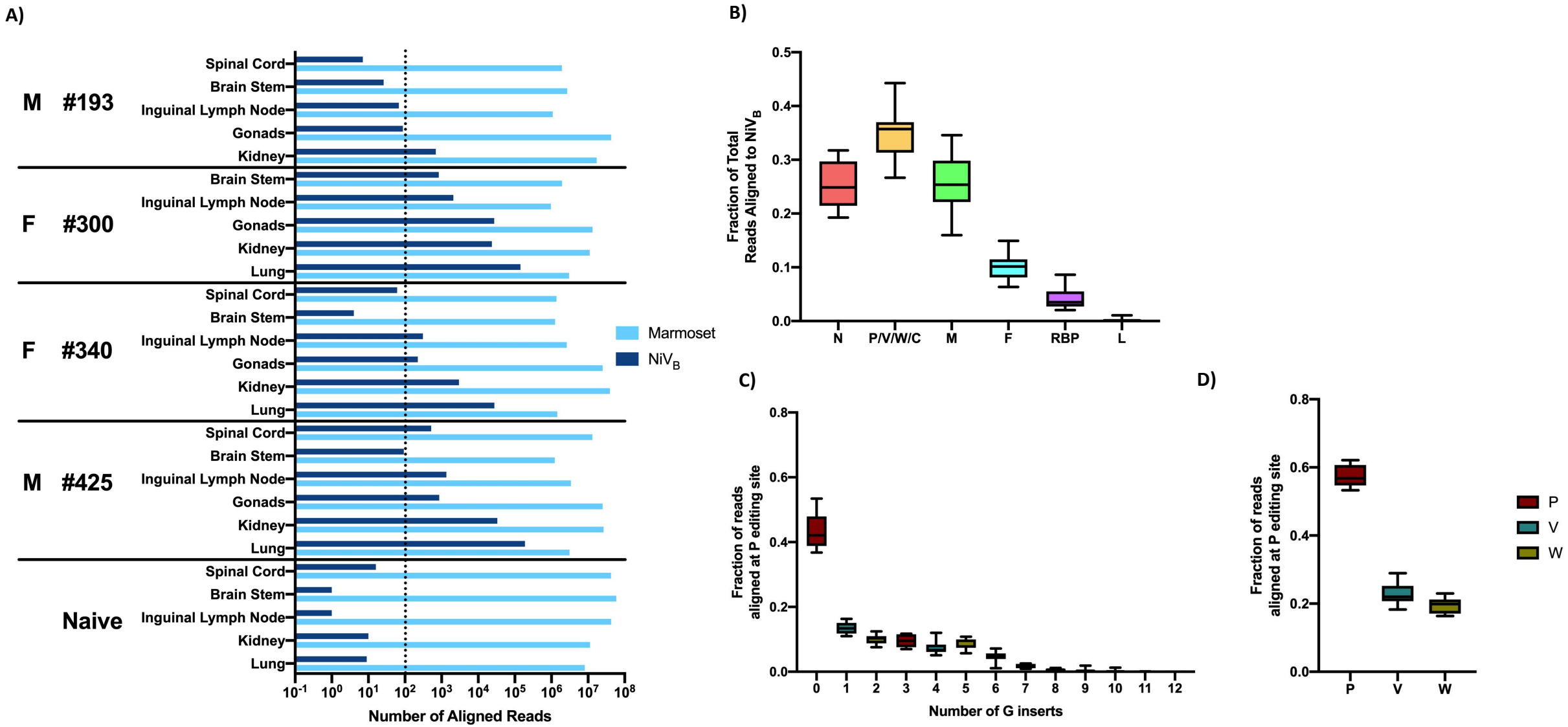

Figure 5. RNA-seq samples aligned to *Callithrix jacchus*.

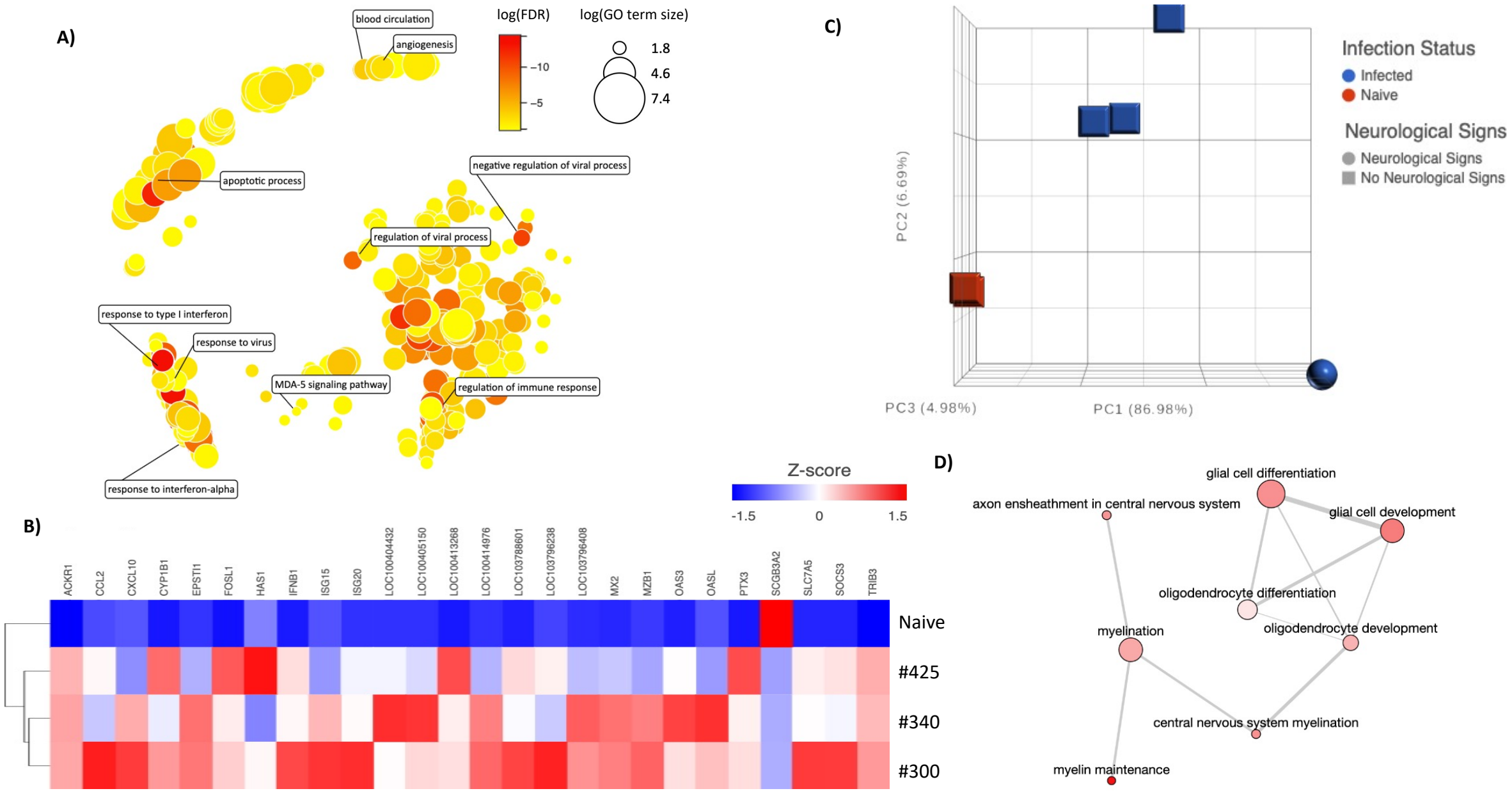

Supplementary Figures

Table S1. Clinical description and diagnosis in NiV_B infected marmosets

Subject No.	Sex	Euthanized (DPI)	Clinical and gross pathology	Clinical diagnosis
193	Male	11	(1) Minimal (<10%) normal lung tissue detected in the cranial portion of the lung. The rest of lung was fluid filled with hemorrhagic/serous fluid. The left and right bronchus had clear fluid present and the trachea had minimal fluid in it. (2) Liver had multi-focal to coalescing regions of pale circles of varying sizes throughout all fields and was very friable. (3) Mediastinal and bronchial lymph nodes had gross enlargement and hemorrhage.	(1) Diffuse Pulmonary Edema and Hemorrhage (2) Diffuse hemorrhagic hepatitis (3) Multi-focal hemorrhagic Lymphadenopathy
300	Female	9	(1) Minimal (<5%) normal lung tissue detected in the cranial portion of the lung. The rest of lung was fluid filled with hemorrhagic/serous fluid. The left and right bronchus had serosanguineous fluid present and the trachea had minimal fluid in it. (2) Liver had multi-focal to coalescing regions of pale circles of varying sizes throughout all fields and was very friable. (3) Inguinal and retropharygneal lymph nodes had gross enlargement but minimal hemorrhage associated with them. (4) Tonsils had pin point hemorrhages associated throughout the tissue. The tissue however was not enlarged. (5) Diffuse subcutaneous liquefactive necrosis of fat. (6) Thoracic cavity contained approximately 1mL of serosanguineous fluid. (7) Peritoneal cavity contained approximately 2mL of serosanguineous fluid.	(1) Diffuse Pulmonary Edema and Hemorrhage (2) Diffuse hemorrhagic hepatitis (3) Multi-focal Lymphadenopathy (4) Hemorrhagic Tonsilitis
340	Female	11	(1) Right lung was normal, though the bronchus was fluid filled. Left lung was congested as it was the dependent lung at the time of death and is a post-mortem change. (2) Liver had multi-focal to coalescing regions of pale circles of varying sizes throughout all fields and was very friable. (3) Inguinal lymph node had gross enlargement but minimal hemorrhage associated with it. (4) Significant hypertrophy of the left ventricular (LV) wall, approximately 10:1 left vs. right. Dilation of the right atrium, though milder than the LV hypertrophy. (5) Infarct was found and malacia near the transition zone between grey and white matter in the occipital lobe of the left cerebral hemisphere. Edema was appreciated in the cerebrum. (6) Trachea was filled with serous fluid at necropsy. (7) Multiple pinpoint areas of hemorrhage were appreciated in the right renal pelvis. (8) Peritoneal cavity contained approximately 0.5 mL of serosanguineous fluid.	(1) Diffuse hemorrhagic hepatitis (2) Left Ventricular Cardiomyopathy / Right Atrial Dilation (3) Cerebral Infarct and malacia in the occipital lobe (4) Cerebral Edema
425	Male	8	(1) Minimal (<5%) normal lung tissue detected in the cranial portion of the lung. The rest of the lung was fluid filled with hemorrhagic/serous fluid. The left and right bronchus had clear fluid present and the trachea had minimal fluid in it. (2) Liver had multi-focal to coalescing regions of pale circles of varying sizes throughout all fields and was very friable. (3) Inguinal, mediastinal and retropharygneal lymph nodes had gross enlargement and hemorrhage. (4) Spleen was extremely friable and congested, no normal tissue was observed on cut sections.	(1) Diffuse Pulmonary Edema and Hemorrhage (2) Diffuse hemorrhagic hepatitis (3) Multi-focal hemorrhagic Lymphadenopathy (4) Splenic Congestion

Supplementary Figure S1. Weight and Temperature.

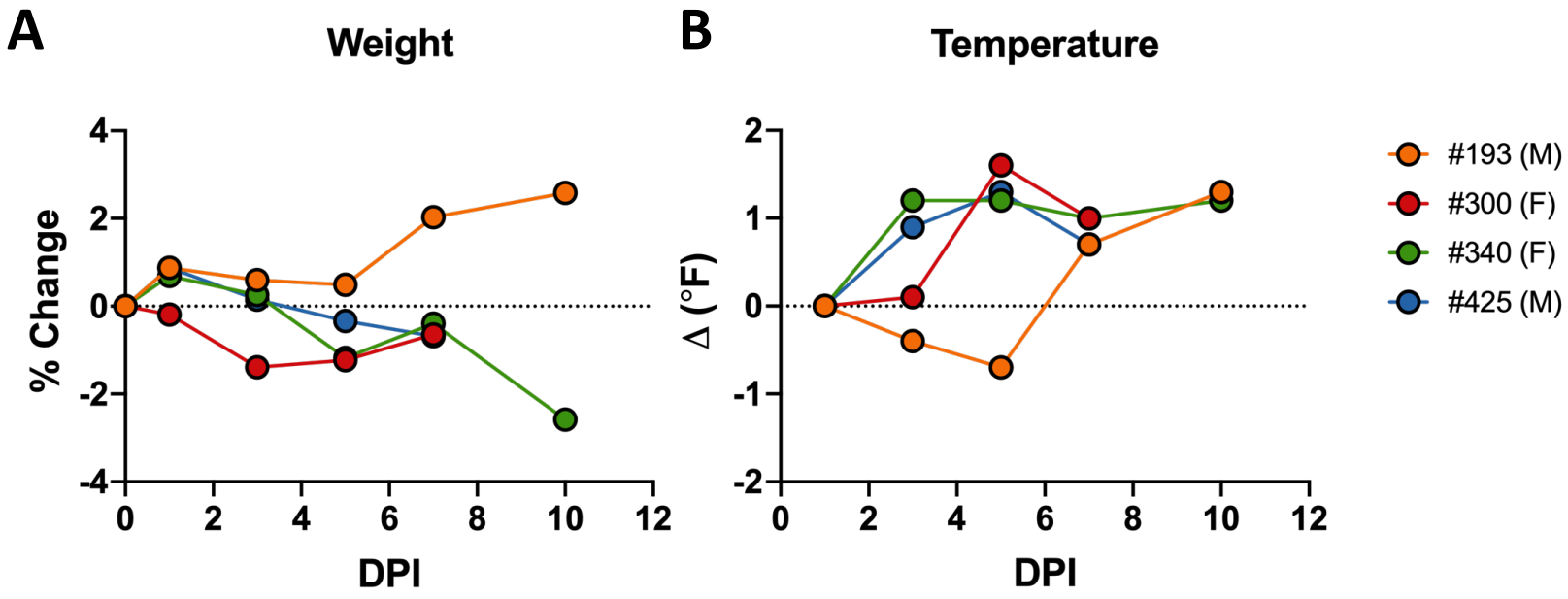

Supplementary Figure S2. X-ray autoradiography.

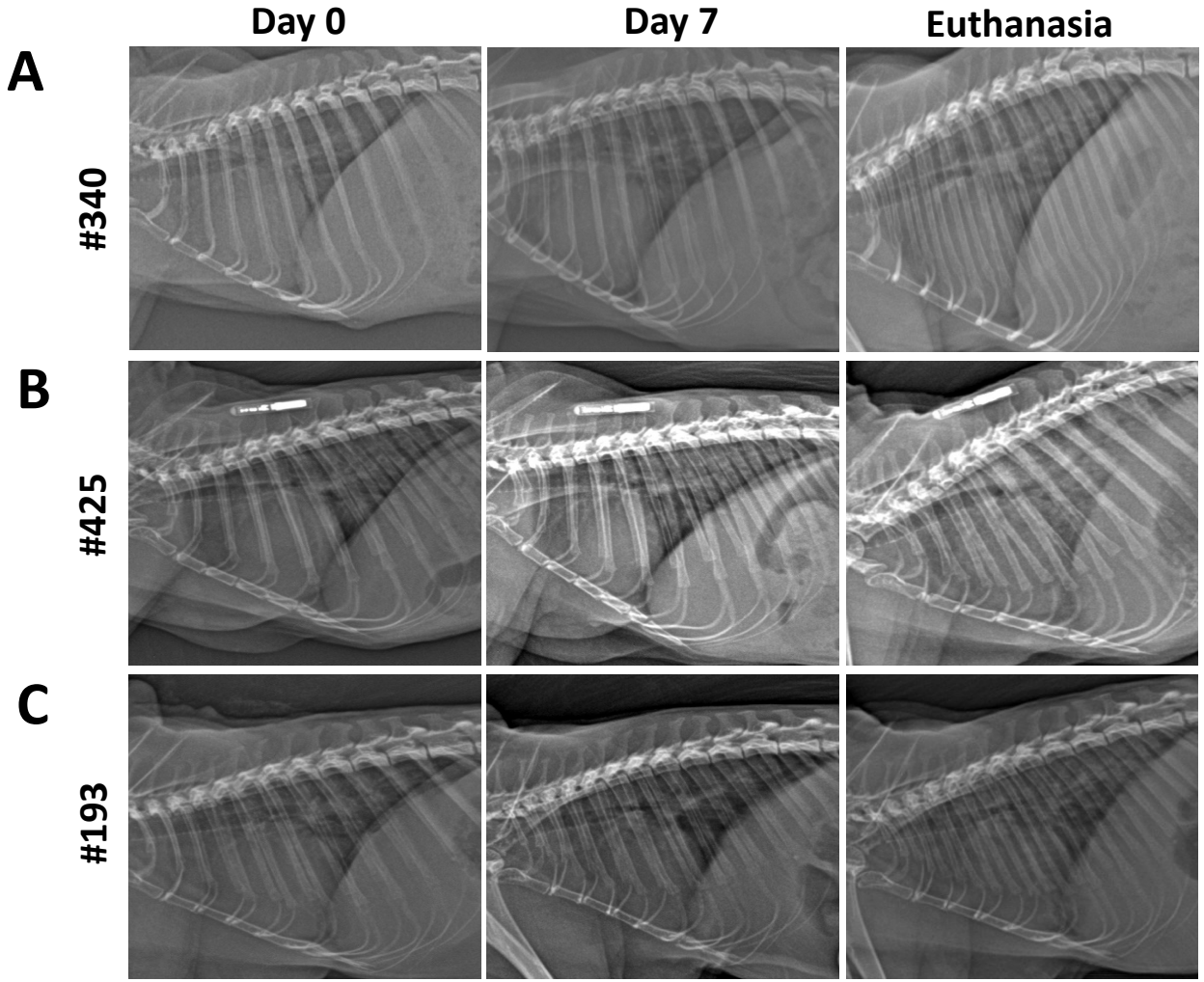

Supplementary Figure S3. Changes in complete blood count.

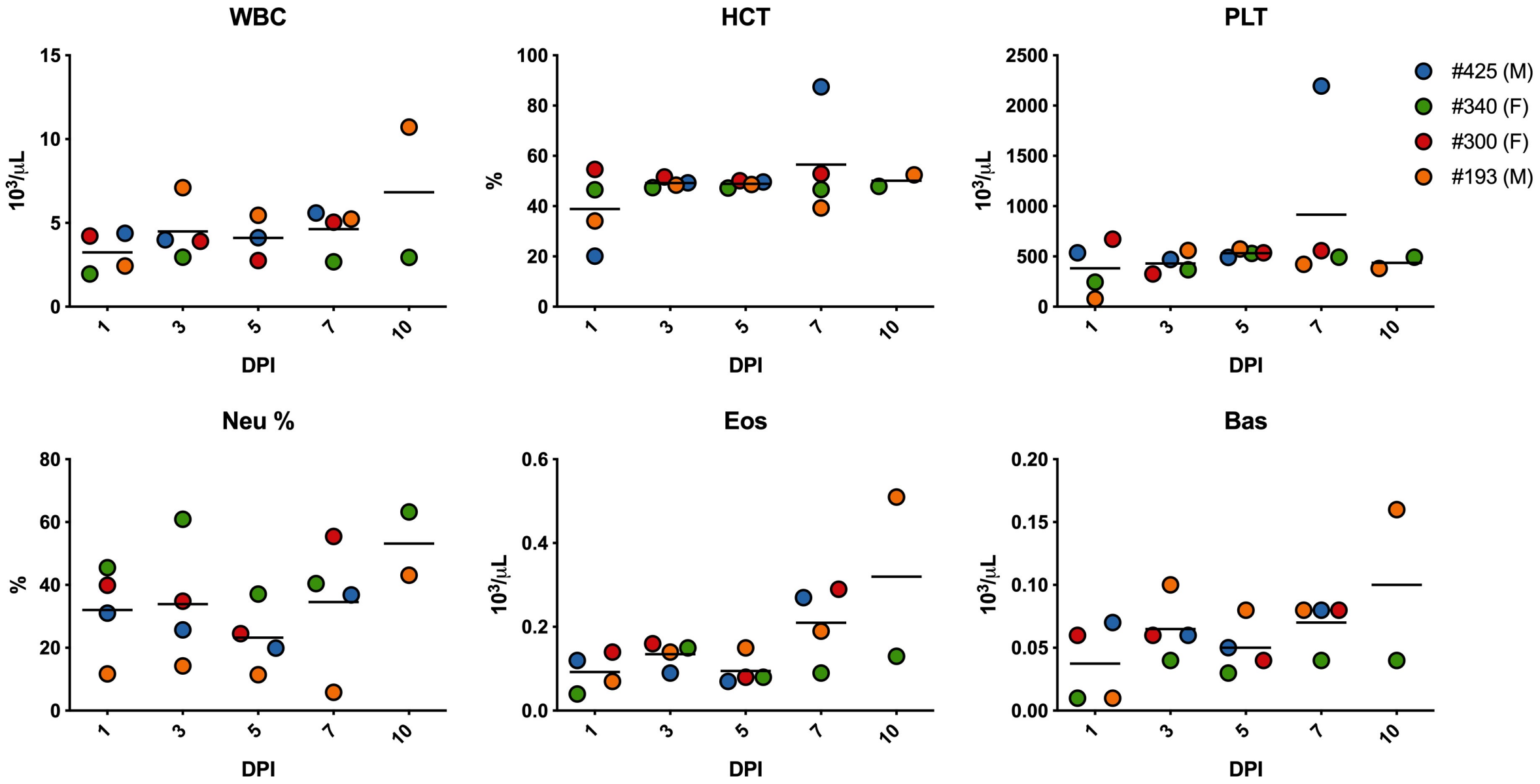

Supplementary Figure S4. Changes in blood chemistry.

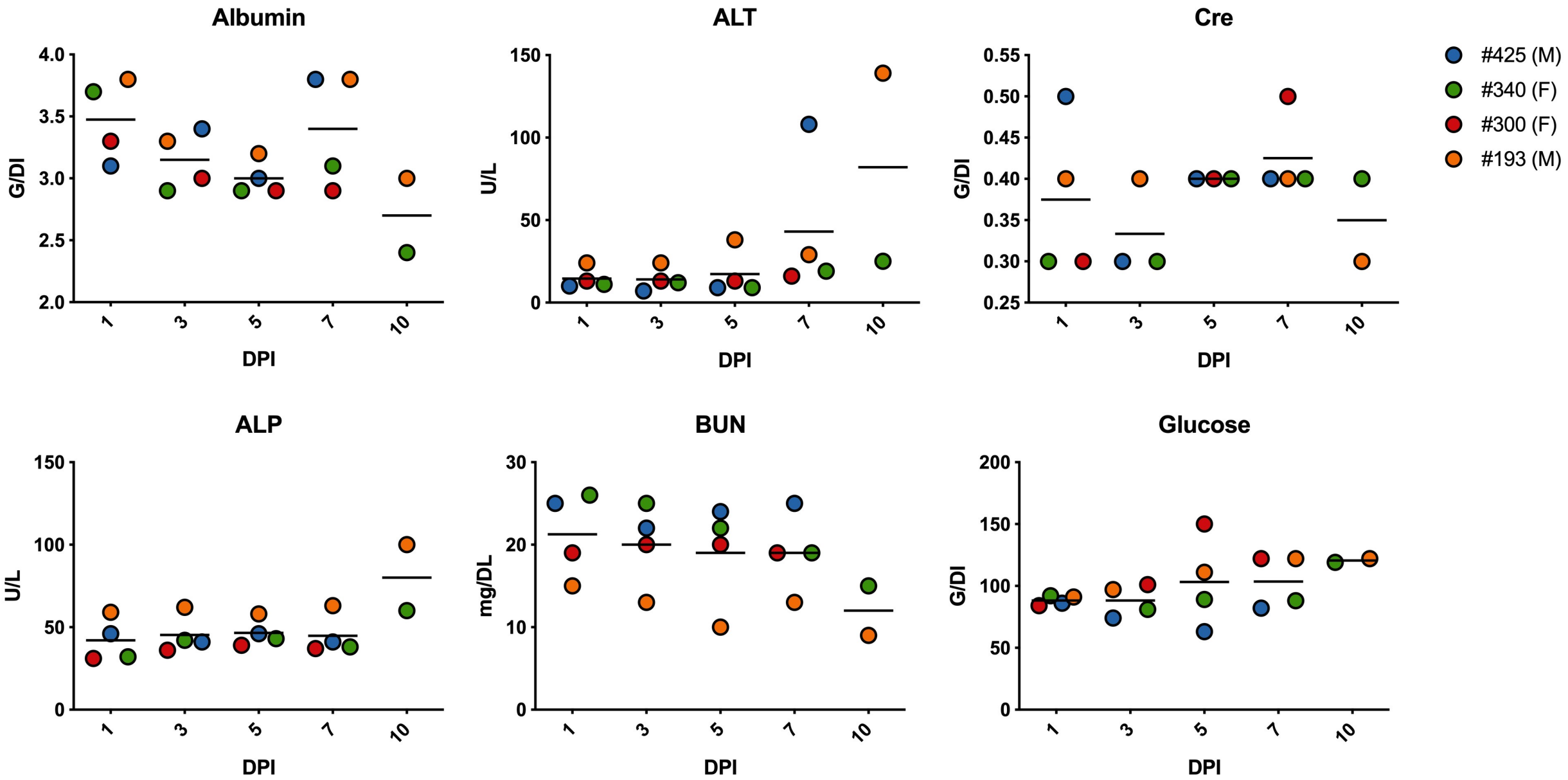

Supplementary Figure S5. Additional changes in complete blood count.

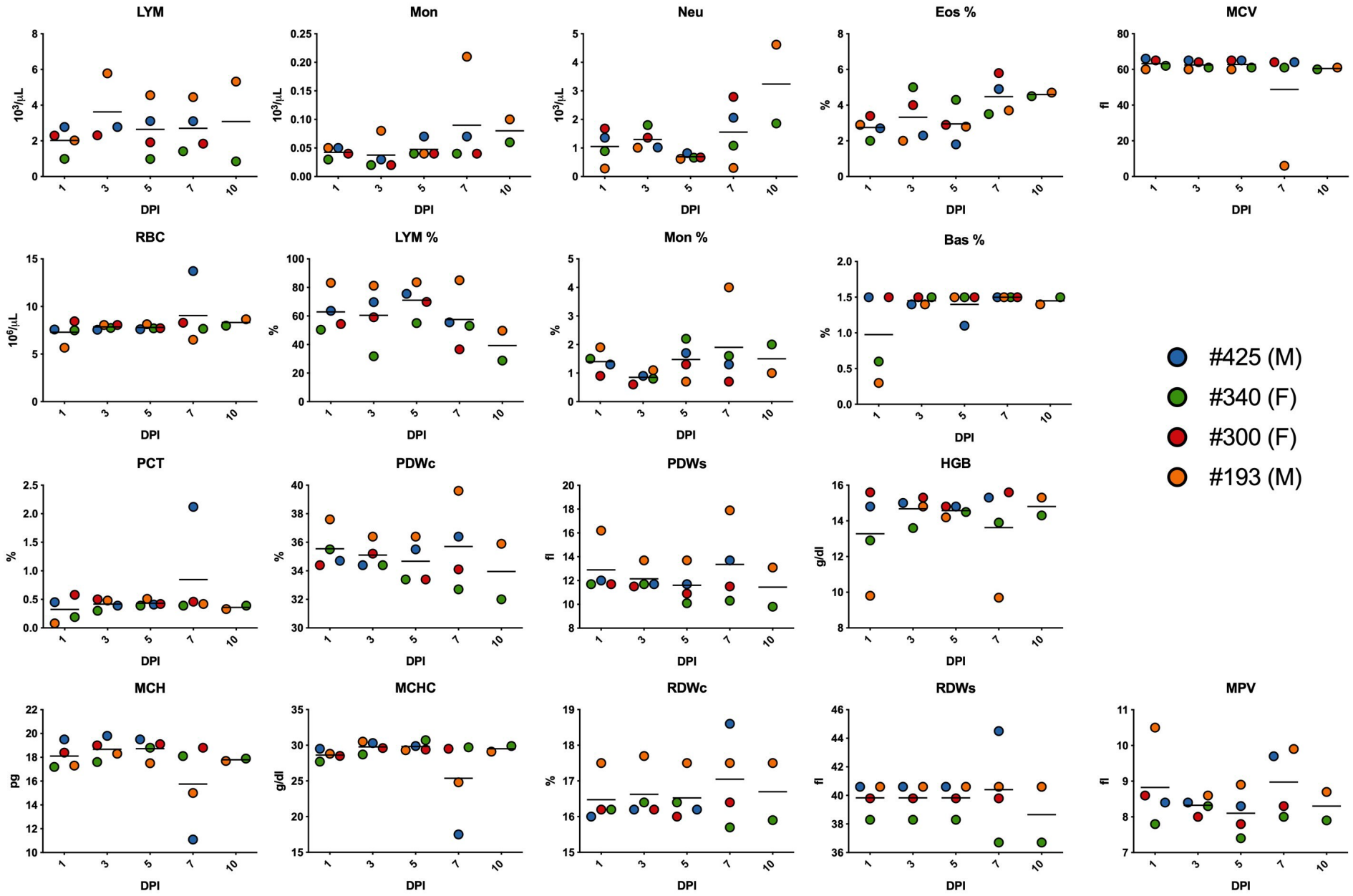
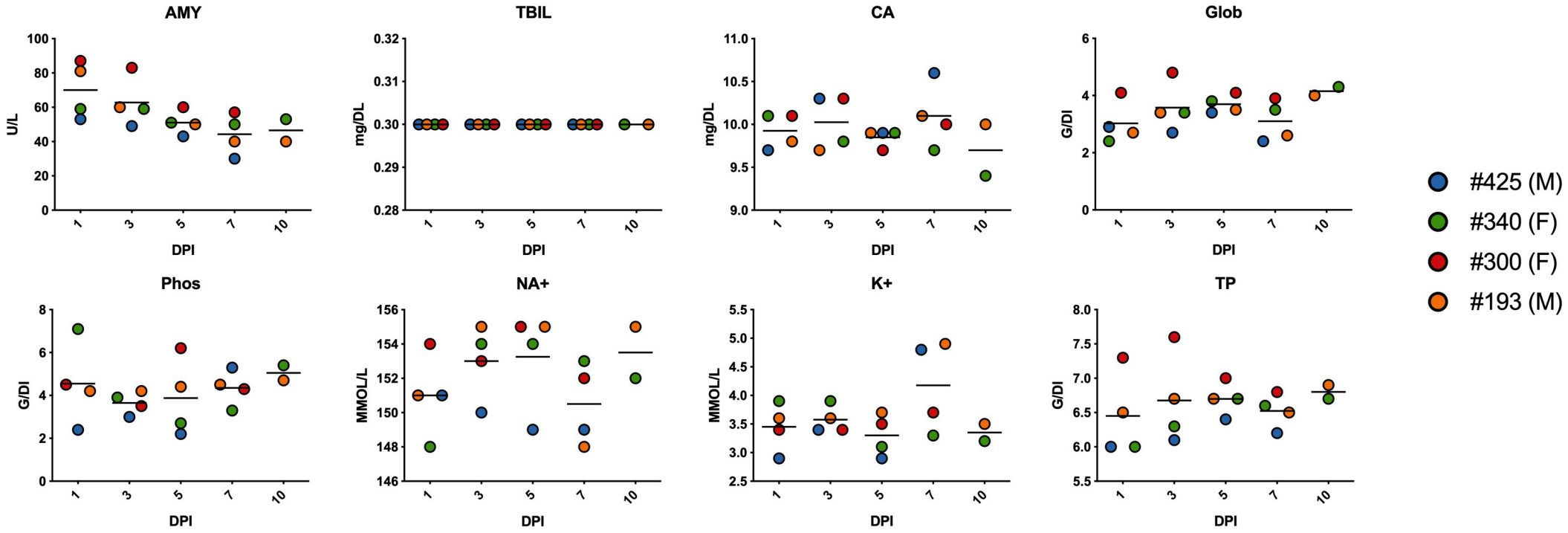
Supplementary Figure S6. Additional changes in blood chemistry.